



Review

# A Review on the Promising Plasma-Assisted Preparation of Electrocatalysts

Feng Yu <sup>1</sup>, Mincong Liu <sup>1</sup>, Cunhua Ma <sup>1</sup>, Lanbo Di <sup>2</sup>, Bin Dai <sup>1,\*</sup> and Lili Zhang <sup>3,\*</sup>

<sup>1</sup> School of Chemistry and Chemical Engineering, Shihezi University, Shihezi 832003, China; yufeng05@mail.ipc.ac.cn (F.Y.); qdulmc@163.com (M.L.); mchua@shzu.edu.cn (C.M.)

<sup>2</sup> College of Physical Science and Technology, Dalian University, Dalian 116622, China; dilanbo@163.com

<sup>3</sup> Institute of Chemical and Engineering Sciences, Agency for Science, Technology and Research, Jurong Island 627833, Singapore

\* Correspondence: db\_tea@shzu.edu.cn (B.D.); zhang\_lili@ices.a-star.edu.sg (L.Z.); Tel.: +86-993-205-7272 (B.D.)

Received: 29 August 2019; Accepted: 3 October 2019; Published: 10 October 2019



**Abstract:** Electrocatalysts are becoming increasingly important for both energy conversion and environmental catalysis. Plasma technology can realize surface etching and heteroatom doping, and generate highly dispersed components and redox species to increase the exposure of the active edge sites so as to improve the surface utilization and catalytic activity. This review summarizes the recent plasma-assisted preparation methods of noble metal catalysts, non-noble metal catalysts, non-metal catalysts, and other electrochemical catalysts, with emphasis on the characteristics of plasma-assisted methods. The influence of the morphology, structure, defect, dopant, and other factors on the catalytic performance of electrocatalysts is discussed.

**Keywords:** electrocatalyst; plasma; defect rich; surface etching; heteroatom doping

## 1. Introduction

Tremendous research efforts have been put to address global energy and environmental concerns. One of the promising energy solutions is electrocatalytic technology, such as fuel cells, the hydrogen production reaction, CO<sub>2</sub> recycling, and ammonia synthesis (Figure 1) [1,2].

Electrocatalytic technology mainly involves two categories: (a) the electrocatalytic oxidation reaction; i.e., the oxygen evolution reaction (OER), hydrogenation reaction (HOR), and methanol oxidation reaction (MOR); and (b) the electrocatalytic reduction reaction; i.e., the oxygen reduction reaction (ORR), CO<sub>2</sub> reduction reaction (CO<sub>2</sub>RR), N<sub>2</sub> reduction reaction (NRR), hydrogen evolution reaction (HER), etc. Electrocatalytic reactions can be carried out at atmospheric temperature and pressure. For example, sustainable ammonia synthesis is achieved under carbon-free conditions using N<sub>2</sub> and H<sub>2</sub>O as the raw materials; the electrochemical reduction of CO<sub>2</sub> is used to prepare chemicals with high energy densities, such as C<sub>1</sub> and C<sub>n</sub>, electrochemically converting electrical energy into an efficient and clean energy carrier-hydrogen energy [3,4]. In addition, chemical energy can be converted into electrical energy using HOR, MOR, or ORR in a fuel cell. ORR and OER can also be used as reversible half-reactions for rechargeable metal-oxygen batteries, using metals, such as Li, Mg, and Zn as energy carriers rather than hydrogen [5].

Currently, noble metal catalysts (such as Au, Pt, Ru, and Ag) are the most important materials for electrocatalysts. They are characterized by easy adsorption of reactants on the surface, the ability to form active intermediates, excellent acid-base corrosion resistance, and outstanding catalytic activity, selectivity, and stability. Compared with noble metal electrocatalysts, inexpensive non-noble metal electrocatalysts also have excellent electrocatalytic performance, especially for transition metal alloys and compounds (oxides, sulfides, nitrides, phosphides, and carbides) [6]. Transition

metals can bond with the reaction molecules to form a transition state with lower energy barrier, thus reducing the activation energy of the whole reaction path and accelerating the chemical reaction [7]. Considering that there are many kinds of non-noble metal electrocatalysts, electrocatalysts with special chemical compositions and physical structures can also be designed and prepared to meet the needs of different electrocatalytic reactions [8]. The excellent acid-base corrosion resistance of non-metallic electrocatalysts have attracted extensive attention of researchers, especially for carbon-based electrocatalysts. Conventional carbon-based molecules have no hollow orbitals, which makes it difficult to participate in the electrocatalytic reaction. However, the electrocatalytic performance of carbon-based materials can be effectively improved by introducing other heteroatoms or functional groups on the surface of carbon materials [9].

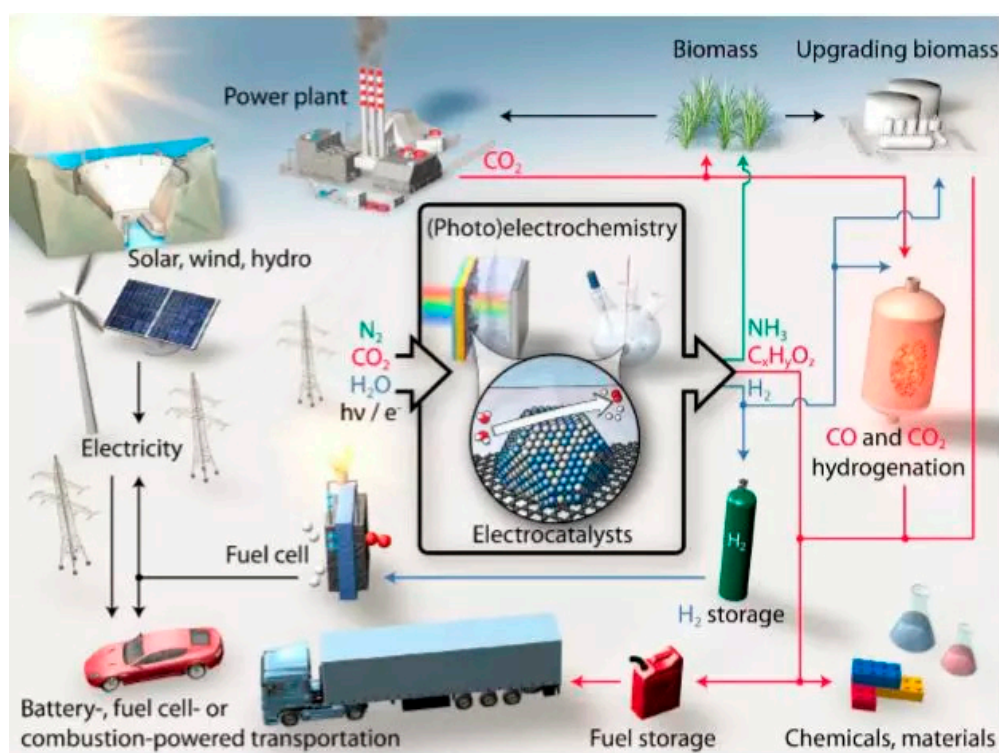


**Figure 1.** The roadmap of electrocatalytic reaction technology for sustainable energy use in the future [1]. (Reproduced with permission from [1]. American Association for the Advancement of Science, 2017).

In recent years, the plasma-assisted preparation method has attracted more and more research interest and has been widely used in the synthesis and modification of electrocatalyst materials. Plasma is partially ionized gas consisting of electrons, ions, molecules, free radicals, photons, and excited species, all of which are active species for the preparation and treatment of catalysts [10]. Differently from the traditional preparation methods, plasma can generate redox species, surface etching, and element doping during the nucleation of catalysts and crystal growth, so as to prepare highly dispersed, small particle size, defect-rich electrocatalysts [11]. This paper reviews the recent progress in plasma-assisted preparation methods, and discusses the effect of plasma on the enhanced catalytic activity through improved dispersion of active species and active sites. Finally, challenges and a future perspective on the development of plasma-assisted preparation of electrocatalysts are provided.

## 2. Noble Metal Electrocatalysts

### 2.1. Plasma Enhanced Deposition

In 1991, Keijser et al. [12], Dutch scientists, first proposed plasma enhanced atomic layer deposition (PEALD) technology. As shown in Figure 2a–c, the common PEALD technologies include direct plasma-enhanced atomic layer deposition, remote plasma-enhanced atomic layer deposition and radical-enhanced atomic layer deposition [13,14]. In 2015, Ting et al. [15] used PEALD technology to deposit Pt nanoparticles with different particle sizes on the TiO<sub>2</sub> surface layer of Ti thin films, and prepared Pt/TiO<sub>2</sub> catalysts. It was found that the average particle size of Pt nanoparticles increased from 3 nm to 7 nm with the increase of deposition times (Figure 2d–i). Pt nanoparticles with a size of ~5 nm exhibited excellent catalytic activity for MOR with the best CO tolerance and electrochemical stability (Table 1), which had potential applications in methanol fuel cells.

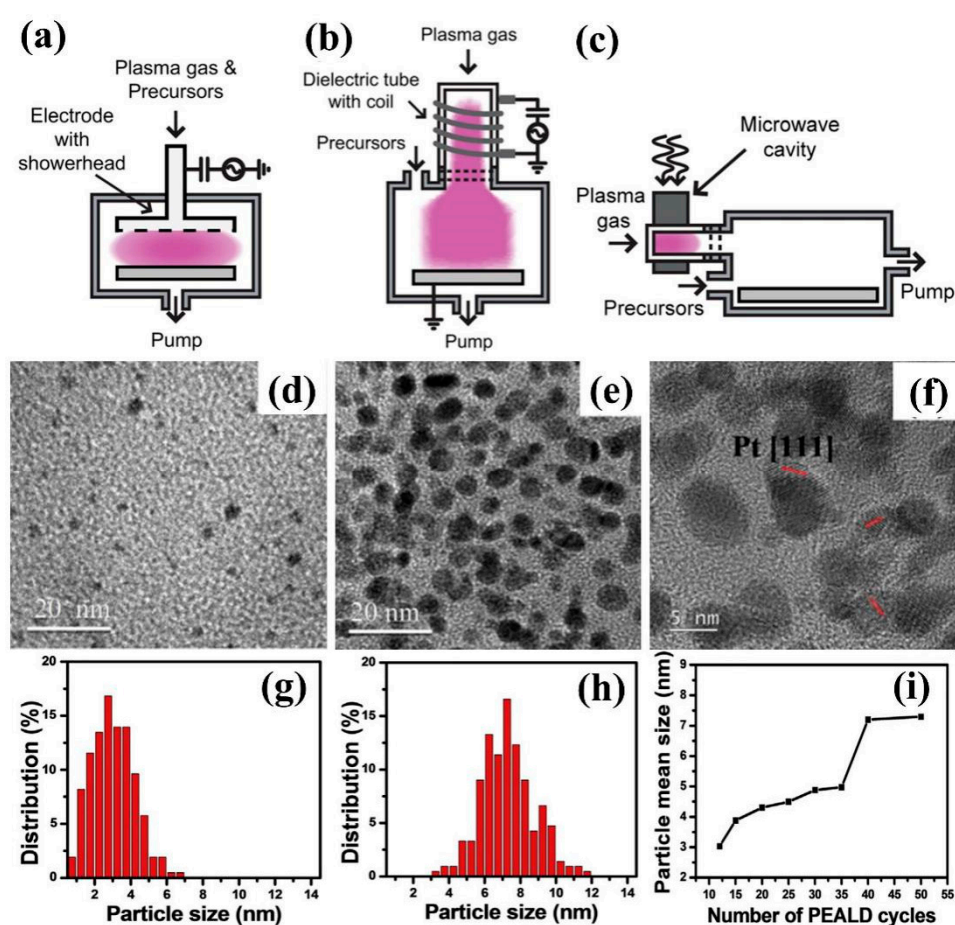


**Figure 2.** Plasma enhanced atomic layer deposition (PEALD) technology (a) direct plasma enhanced atomic layer deposition; (b) remote plasma enhanced atomic layer deposition; (c) radical-enhanced atomic layer deposition [13] (Reproduced with permission from [13], American Vacuum Society, 2007.) HRTEM images of samples with different PEALD deposition times: (d) 12 times, (e) 50 times, and (f) 40 times. Corresponding particle size distribution maps: (g) 12 times and (h) 50 times. (i) The graph of relationship between the average particle size distribution and the number of depositions [15]. (Reproduced with permission from [15]. Elsevier B.V., 2015).

In the same year, Yoshiaki et al. [16] produced highly ionized metal plasma by coaxial pulse arc plasma deposition (CAPD), which deposited Pt nanoparticles with average particle diameter of 2.5 nm on the carbon carrier (Ketjenblack carbon). Compared with the commercial 20% Pt/C, the catalytic activity and stability of the catalysts were significantly improved for MOR. Moreover, the catalysts

exhibited excellent initial potential and half-wave potential for ORR performance. The half-wave potential was 0.87 V, which was higher than that of 5% Pt/C (0.78 V) and 20% Pt/C catalysts (0.84 V).

Plasma sputtering (IPS) is also used to prepare noble metal electrocatalysts. Grigoriev et al. [17] used Cabot carbon black (Vulcan XC-72), carbon nanotubes and nanofibers as substrates to deposit Pt and PtPd nanoparticles, which had potential electrochemical activity in fuel cells, water electrolysis cells and dual-function fuel cells. Falch et al. [18] deposited then Pt<sub>x</sub>Pd<sub>y</sub> film on SiO<sub>2</sub> substrates by magnetron enhanced plasma sputtering. It was found that Pt<sub>3</sub>Pd<sub>2</sub> and PtPd<sub>4</sub> exhibited good catalytic activity in the electrocatalytic oxidation of SO<sub>2</sub>. Compared with pure platinum (0.598 + 0.011 V, standard hydrogen electrode (SHE)), those two thin film materials had lower initial potential (0.587 + 0.004 V, SHE), which showed their potential application in SO<sub>2</sub> oxidation.

## 2.2. Gas Plasma-Assisted Preparation

Plasma is a high energy state gas with electrons, ions, and free radicals. Common gases can be used to form plasma, such as H<sub>2</sub>, O<sub>2</sub>, CO<sub>2</sub>, Ar, NH<sub>3</sub>, and N<sub>2</sub>. When high energy plasma gas gets into contact with the surface of the material, it will lead to the physical and chemical changes of the material surface, such as chemical reduction, surface etching, the generation of surface active groups, etc. [19] In 2018, Ma et al. [20] irradiated Pt-based catalysts with high-energy electrons and activated ions in H<sub>2</sub> plasma, which could simultaneously reduce Pt ions and graphene oxide (GO), as shown in Figure 3a. By adjusting the mass ratio of GO to multi-walled carbon nanotubes (MWCNT), Pt nanoparticles with different particle size distribution were obtained (Figure 3b–e). Pt/GNT had excellent MOR performance and anti-poisoning performance. The current density of Pt/GNT was 97.9 mA/mg, which was 2.2 times higher than that of commercial Pt/C (44.1 mA/mg). The current density of Pt/GNT was 691.1 mA/mg, which was much higher than that of commercial Pt/C (368.2 mA/mg).

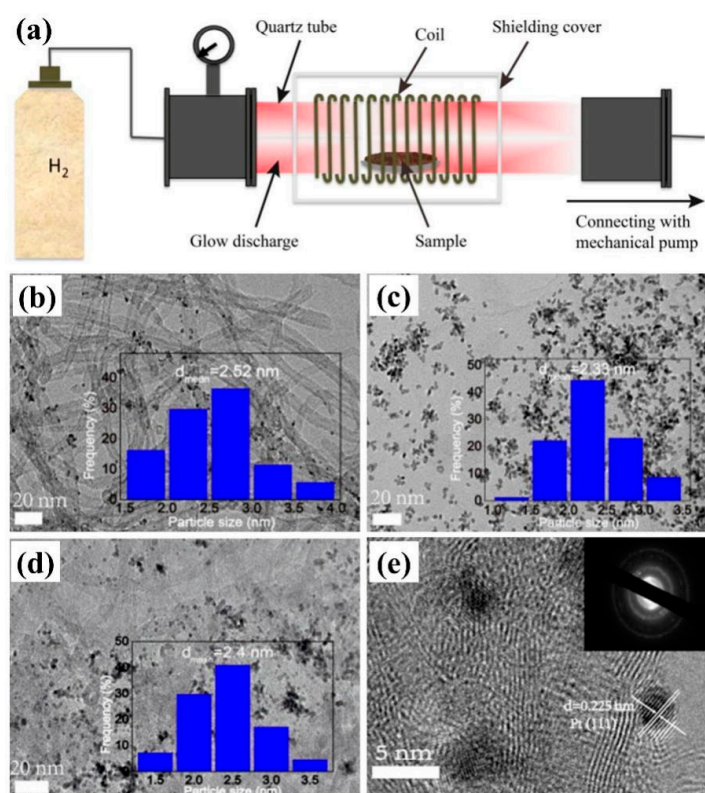


**Figure 3.** (a) The sketch of device for sample treatment by H<sub>2</sub> plasma. TEM images and corresponding Pt particle size distribution images: (b) Pt/carbon nanotubes (CNTs), (c) Pt/RGO, and (d) Pt/GNT (graphene oxide (GO):CNTs = 1:2, mass ratio). (e) HRTEM and SAED images of Pt/GNT [20]. (Reproduced with permission from [20]. Elsevier B.V., 2018).

By contrast, Xu et al. [21] found that Pt nanoparticles in Pt/CNTs-HP prepared by H<sub>2</sub> plasma reduction of Pt-based precursor showed more uniform distribution on CNT with the particle size of about 2 nm. They had better MOR electrocatalytic activity than a traditional hydrogen reduced catalyst (Pt/CNTs-H) and NaBH<sub>4</sub> reduced catalyst (Pt/CNTs-N). Precursors of noble metal catalysts can also be reduced by Ar plasma. Sui et al. [22] obtained Pt-Ir/TiC bimetallic electrocatalysts by Ar plasma reduction method, which had finer metal crystals and higher metal dispersion. The bimetallic electrocatalyst showed higher ORR/OER catalytic activity than that of the Pt-Ir/TiC electrocatalysts prepared by chemical reduction method.

Gas plasma can also be used to treat noble metal catalysts directly. Ipshtita et al. [23] treated the Au@Pt catalyst with Pt loading of 1.75 ug/cm<sup>2</sup> (corresponding to two layers of Pt atoms covering a gold core with a diameter of 5 nm) by Ar plasma. It was found that Ar plasma can enhance the formation of highly active Pt (110) crystal face. The total surface area was as high as 48 ± 3 m<sup>2</sup>/g, which was equivalent to 44% of the utilization rate of Pt atoms. The catalysts exhibited excellent CO poisoning resistance and outstanding MOR and ORR properties. Koh et al. [24] prepared “Au Islands” catalysts by treating gold foil with O<sub>2</sub> plasma, which showed excellent CO<sub>2</sub>RR performance. Compared with polycrystalline gold electrode, the “Au Islands” catalysts had excellent CO selectivity, and their Faraday efficiency was more than 95%, which attracted people’s attention.

### 2.3. Solution Plasma Sputtering

Solution plasma sputtering (SPS) can occur between electrodes and solutions, providing a new plasma-liquid interface that initiates a variety of physical and chemical processes, as shown in Figure 4a,b. The unique interaction can be used to prepare noble metal nanoparticles and to promote carbon aggregation, so as to produce excellent electrocatalysts [25,26]. Kim et al. [27] obtained metal filtrate through corrosion of electrodes by discharging in water with pulsed plasma. Pt and Pt-M (M = Cu, Ag and Pd) bimetallic nanoparticles were prepared, which had no element segregation or phase segregation during the alloying of Pt and M. Among them, Pt-Ag bimetallic nanoparticles exhibited excellent MOR electrocatalytic activity, stability, and durability. At the same time, Kim et al. [28] pointed out that the corrosion of anode electrode was more aggressive than that of cathode electrode during plasma discharge, and the composition of Pt-Pd bimetallic nanoparticles can be varied with power and electrode structures. Cho et al. [29] found that Pt<sub>69</sub>Pd<sub>31</sub> had excellent catalytic activity for MOR, with a current density of 6.81 mA/cm<sup>2</sup>, making it an ideal candidate catalyst for methanol fuel cell.

Metal-carbon composites can be obtained by adding carbon materials to the metal filtrate prepared by SPS. In 2017, Zhang et al. [30] used SPS technology to synthesize PtPd filtrate directly from Pt and Pd wire, and then Koqin black carbon material was added to obtain PtPd/C. As shown in Figure 4c-f, PtPd/KB-2 prepared in a mixture of methanol and water had better dispersion of metal particles than that prepared in water. The particle diameter was about 2–5 nm. The MOR activity of PtPd/KB-2 (12 wt% Pt) was four times better than that of commercial Pt/C catalyst, and the electrochemical surface area was 2.5 times of that of commercial Pt/C catalyst. Meanwhile, the mass activity of PtPd/KB-2 after 300 cycles can reach 43%. In 2018, Horiguchi et al. [31] designed a SPS mobile cell, which can continuously add Vulcan XC72R to the solution containing Pt to prepare Pt/XC72 electrocatalysts, providing a new route for the continuous production of electrocatalysts.

Metal-carbon composites can also be obtained by placing metal nanoparticles prepared by SPS in uniformly dispersed carbon-containing suspension. In 2017, Huang et al. [32] acquired Pt/CoPt/MWCNTs composite catalysts by dispersing Pt/CoPt composite nanoparticles by SPS in a uniform aqueous solution of multi-walled carbon nanotubes (MWCNT). The electrocatalysts exhibited excellent MOR catalytic activity and good stability, which exhibited an activity of 1719 mA/mg<sub>Pt</sub> 3.16 times higher than that of commercial Pt/C. It can be used as a catalyst for direct methanol fuel cell. Su et al. [33] prepared Pt nanoparticles with particle size of 2 nm by SPS in a XC72 suspension. Pt/C/TiO<sub>2</sub> electrocatalysts were then synthesized by mixing the obtained Pt/C composites with TiO<sub>2</sub> nanotubes

under ultrasound. The catalysts showed good electrocatalytic activity, and the CO toxicity resistance of the current density was 315.2 mA/mg, which is 1.73 times higher than that of commercial Pt/C.

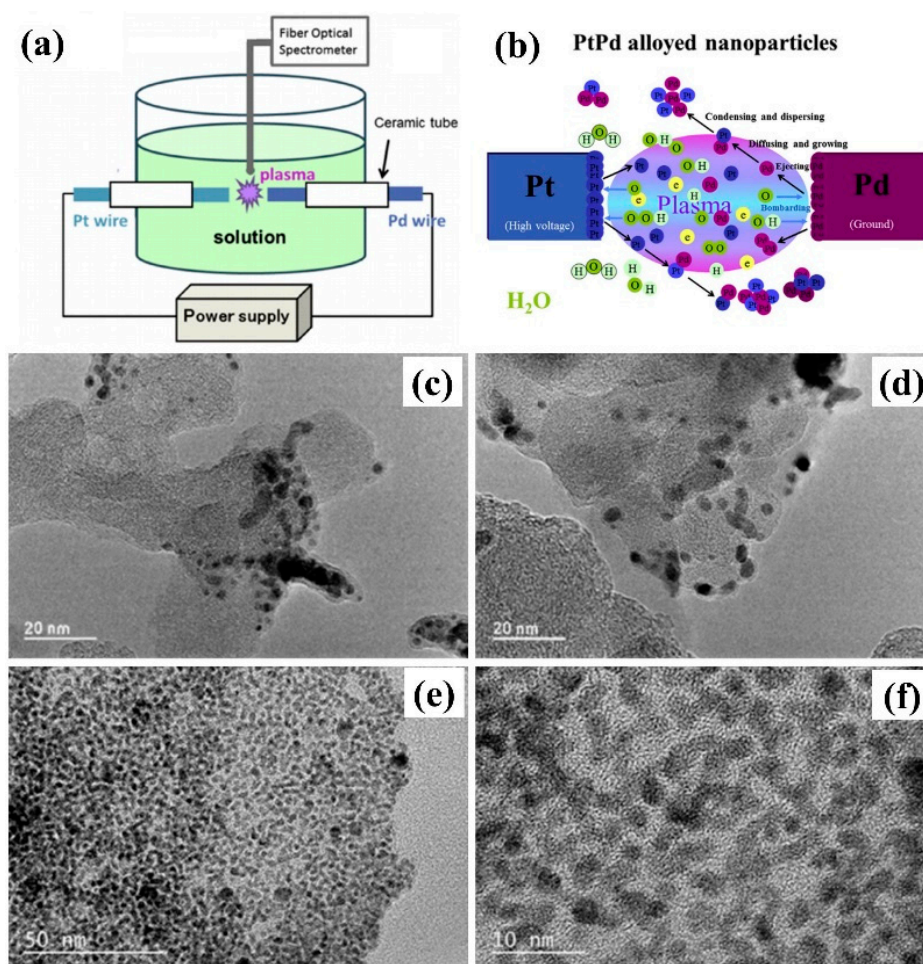


**Figure 4.** (a) The experimental device and (b) the schematic diagram of PtPd nanoparticles synthesized by solution plasma sputtering. Catalysts formed in different solutions: (c,d) PtPd/KB in aqueous solution; (e,f) PtPd/KB-2 in water-methanol mixture [30]. (Reproduced with permission from [30]. Elsevier B.V., 2017).

Besides, the carbon-containing suspension can be used instead of water or alcohol solvents to prepare carbon-supported precious metal electrocatalysts. Hu et al. [34] successfully prepared PdAu/KB electrocatalysts by plasma discharge in the suspension of Keqin black carbon material using Pd and Au wires as electrodes. PdAu alloy nanoparticles with an average particle size of 2–5 nm were uniformly distributed on KB, and exhibited outstanding ORR activity in an acidic solution (0.5 M H<sub>2</sub>SO<sub>4</sub>, 240 cycles) and an alkaline solution (0.5 M NaOH, 700 cycles). As electrocatalysts, PdAu alloy nanoparticles have potential applications in future fuel cells or metal air batteries.

In addition to water or alcohol solvents, carbon-supported noble metal electrocatalysts can be directly obtained by using organic solutions as liquid plasma discharge media. As shown in Figure 5a–b, carbon nanospheres (CNS) can be formed when benzene is used as an organic solvent in plasma discharge. At the same time, metal nanoparticles (such as Au and Pt) produced by metal electrode sputtering are deposited on carbon nanospheres to obtain highly active electrocatalysts, loaded with precious metal nanoparticles. At the same time, the metal nanoparticles (Au, Pt, etc.) produced by metal electrode sputtering can be loaded on carbon nanospheres to obtain highly active carbon-supported noble metal nanoparticles electrocatalysts [35,36]. The carbon nanospheres obtained

by this method exhibited a diameter range of 20 to 30 nm and a pore size range of 13 to 16 nm. The Au nanoparticles had a particle diameter of less than 10 nm and were uniformly dispersed on the carbon nanospheres (Figure 5c–e), making them an ideal carbon-supported, noble metal electrocatalyst.

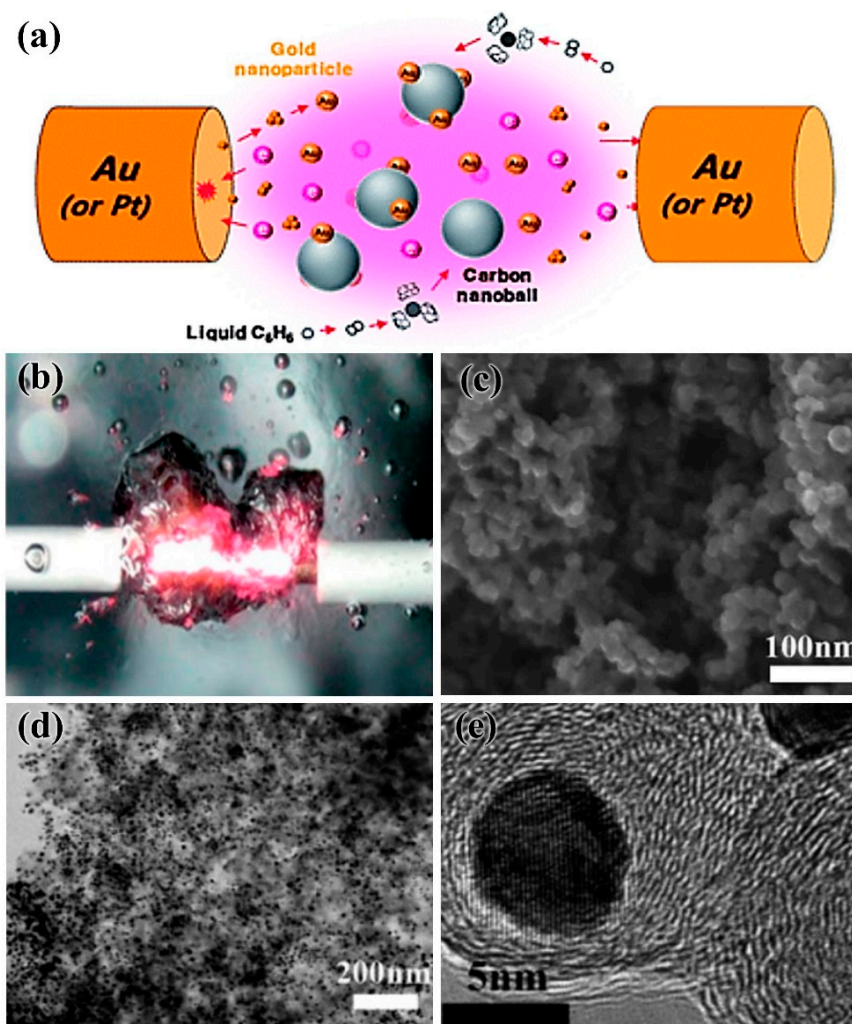


**Figure 5.** (a) The schematic diagram and (b) the physical diagram of carbon-loaded noble metal materials prepared by organic solution plasma. (c) Field emission scanning electron microscope (FESEM), (d) scanning transmission electron microscope (STEM), and (e) HRTEM diagrams of Au/CNPs catalysts [35]. (Reproduced with permission from [35]. Royal Society of Chemistry, 2013).

Solution plasma process can also directly reduce noble metals to prepare electrocatalysts [37]. Lee et al. [38] synthesized Pt/C electrocatalysts with Pt nanoparticles being reduced by  $\text{H}_2\text{PtCl}_6 \cdot 6\text{H}_2\text{O}$ , while carbon supports were formed by the corrosion of carbon electrodes during the solution plasma process. The Pt nanoparticles with a diameter of about 38.14 nm were composed of many primary particles with a diameter of about 1.85 nm, which exposed more (111) crystal faces and exhibited good HOR catalytic activity. In 2018, Hussain et al. [39] used He/ $\text{H}_2$  plasma to reduce  $\text{H}_2\text{PtCl}_6$  to Pt nanoparticles which were then loaded on nitrogen-doped reduced graphene oxide (rGO-N). The obtained Pt/rGO-N electrocatalysts showed a comparable high ORR electrocatalytic activity and superior stability to the commercial Pt/C. It was found that the ORR activity in the electrolytes of 0.1 M KOH and 0.05 M  $\text{H}_2\text{SO}_4$  were three and two times higher than that in commercial Pt/C, respectively. Cui et al. [40] prepared  $\text{PtO}_a\text{PdO}_b @ \text{Ti}_3\text{C}_2\text{T}_x$  catalysts by loading PtPd bimetallic oxide nanoparticles onto two-dimensional MXene carrier by solution plasma reduction, as shown in Figure 6. The particle size of PtPd nanoparticles increased with the extension of plasma reaction time. The catalyst obtained

by plasma reaction for 3 min showed good catalytic activity for HER and OER, exhibiting the activation potential of HER in 0.5 M  $\text{H}_2\text{SO}_4$  of 57 mV, which was the same for that of OER in a 0.1 M KOH solution of 1.54 V at the current density of 10  $\text{mA}/\text{cm}^2$ . In particular, it had superior water electrolysis performance in an alkaline solution of 1.0 M KOH, which showed that the electrolysis water voltage at the current density of 10  $\text{mA}/\text{cm}^2$  was 1.53 V.

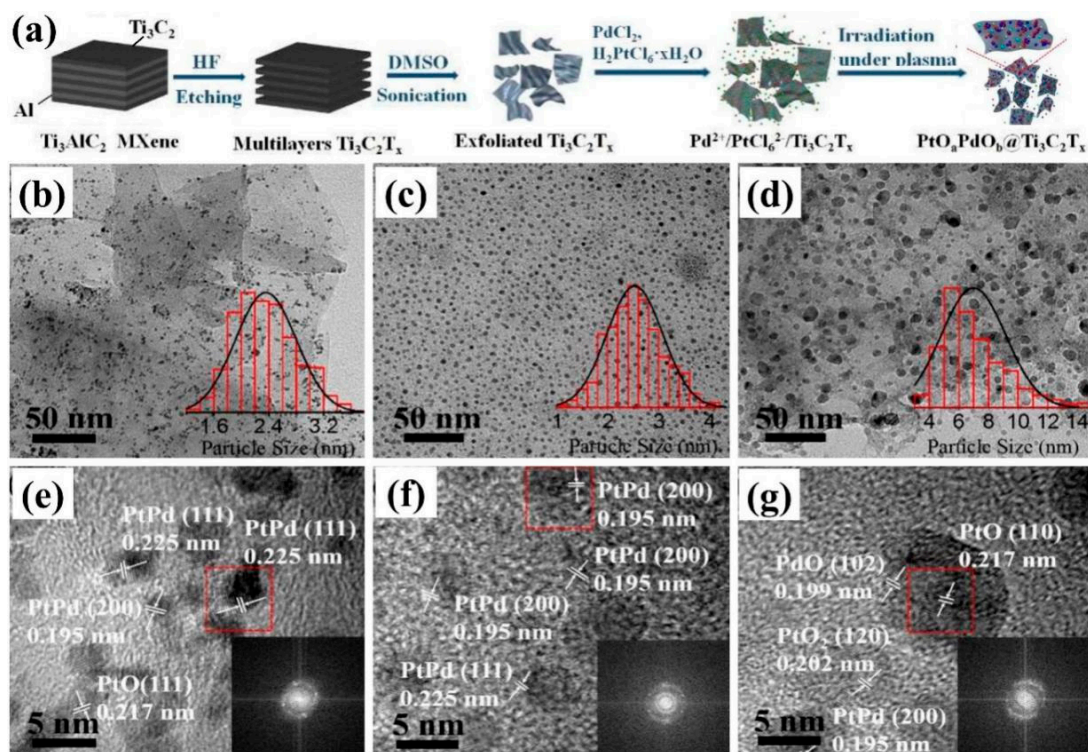


**Figure 6.** (a) The flow chart of  $\text{PtO}_x\text{PdO}_y@\text{Ti}_3\text{C}_2\text{T}_x$  catalysts prepared by liquid plasma reduction. TEM and HRTEM images with 200 W plasma for (b,e) 1 min, (c,f) 3 min, and (d,g) 5 min. (e–g) corresponding fast fourier transform (FFT) diffraction patterns [40]. (Reproduced with permission from [40]. American Chemical Society, 2018).

#### 2.4. Plasma Prepared and Modified Electrocatalysts Support

Plasma technology is also used to prepare and modify the catalyst carrier that achieves hydrophilicity and element doping, and promote the dispersion of the catalyst's active components and the improvement of its catalytic activity [41–43]. Chetty et al. [44] formed abundant CO and COO-functional groups on the surface of multi-walled carbon nanotubes (CNT) by  $\text{O}_2$  plasma, which improved the dispersion of Pt-Ru nanoparticles and the catalytic activity toward MOR. Ding et al. [45] prepared N-doped graphene-coated Pt nanocrystals (N-GPN) by  $\text{N}_2$  plasma treatment of GPN (Figure 7a–f). From Figure 7g–h, it can be seen that nitrogen doping can produce more active sites and improve the electrocatalytic performance for ORR, which can effectively regulate the activity of the electrocatalysts. Loganathan et al. [46] prepared different Pt/C(N) and Pt/C(AA) catalysts with excellent ORR catalytic activities by modifying carbon black used for the fuel cell catalyst support system with  $\text{N}_2$  and allylamine plasma, respectively. Du et al. [47] realized in-situ N-doping and surface modification on carbon paper carrier surface by 25%  $\text{N}_2$  + 75%  $\text{H}_2$  plasma treatment, promoting the growth of Pt nanowire arrays (NW). The self-supporting Pt NW/GDL (large area gas diffusion layer) electrocatalysts with an area of 5  $\text{cm}^2$ , could be directly used as catalyst electrodes for fuel cells, which showed excellent charge transfer and mass transfer properties, and their power density was twice as high as that of traditional Pt nanoparticles.



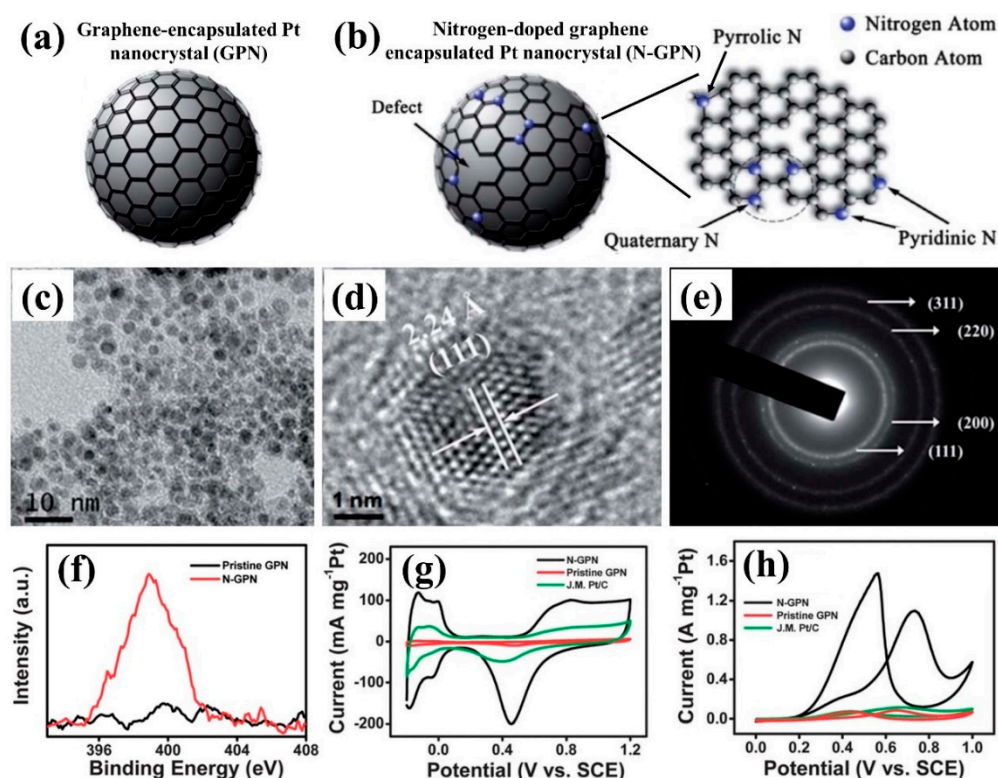


**Figure 7.** The schematic diagram of (a) graphene-supported Pt nanoparticles (GPN) and (b) N-doped GPN (N-GPN); The images of (c) TEM, (d) HRTEM, and (e) selected area electron diffraction (SAED) for GPN; (f) XPS image; (g) chemical vapor (CV)—0.5 M H<sub>2</sub>SO<sub>4</sub>, and (h) CV—0.5 M H<sub>2</sub>SO<sub>4</sub> + 1.0 M CH<sub>3</sub>OH for GPN and N-GPN [45]. (Reproduced with permission from [45]. American Chemical Society, 2014).

In 2017, Hu et al. [48] obtained Pt/ZnO/KB photocatalysts with solution plasma technology. They first synthesized ZnO nanowires using zinc electrode wires, and then replaced them with Pt electrode wires, loaded Pt nanoparticles onto zinc oxide, and finally, placed Pt/ZnO in Keqin black suspension to obtain a Pt/ZnO/KB photocatalyst. Pt/ZnO/KB exhibited excellent MOR photocatalytic activity due to the better electron transport performance and smaller resistance of ZnO nanowires. The catalytic activity of Pt/ZnO/KB was 964 mA/mg, which was more than three times that of Pt/KB (306 mA/mg). Meanwhile Pt/ZnO/KB showed excellent CO toxicity resistance and stability, which made it possible for methanol fuel cells to work all-weather in light or dark.

### 3. Non-Noble Metal Electrocatalysts

#### 3.1. Metal and Alloy Electrocatalysts

In recent years, non-noble metal catalysts have attracted more and more attention. In particular, transition metals with empty orbitals combined with molecules containing lone pairs of electrons through coordination bonds to form transition states with lower barriers reduce the activation energy of the whole reaction path and accelerate the chemical reaction. In 2016, Flis-Kabulska et al. [49] prepared Ni-Fe-C electrocatalysts by introducing carbon into NiFe alloy using CH<sub>4</sub>+H<sub>2</sub> plasma carburization. Although the solubility of carbon in NiFe alloy was very low, a carbide layer with thickness of about 2 μm was formed on the surface, which greatly improved the surface hardness and corrosion resistance. Ni-Fe-C alloy exhibited good HER catalytic activity in 25 wt.% KOH solution at 80 °C. Jin et al. [50] used the microwave plasma chemical vapor deposition (MPECVD) method to coat carbon nanoparticles on carbon cloth, which prepared a three-dimensional CoNPs@C with excellent conductivity and catalytic activity. It was found that a low overpotential of 153 mV can be generated at the current density of

10 mA/cm<sup>2</sup> for HER, and the overpotential was 270 mV for OER, and the decomposition voltage was 1.65 V when composing a full hydrolyzed cell.

Cu-based catalysts are commonly used in the preparation of hydrocarbons by CO<sub>2</sub>RR, such as carbon monoxide, methane, ethylene, ethanol, and n-propanol [51]. Mistry et al. [52] used plasma to treat oxidized Cu-based catalysts for the catalytic reduction of CO<sub>2</sub> at low overpotential. It can be seen from Figure 8a–h that Cu<sub>2</sub>O was not completely reduced during the reaction, and Cu<sup>+</sup> ions were still on the surface. Cu-based catalysts derived from oxides only had a minimal effect on catalytic performance, while Cu<sup>+</sup> played an important role in reducing the initial potential and improving the selectivity of ethylene. Among the catalysts, Cu foil treated by O<sub>2</sub> plasma had 60% ethylene selectivity at −0.9 V (versus reversible hydrogen electrode (RHE)) potential (Figure 8i,j). In 2017, Gao et al. [53] adjusted Cu (100) crystal face and the content of oxygen/chloride ion by treatment of Cu nanoparticles with H<sub>2</sub>, O<sub>2</sub>, and Ar plasma, respectively. It was found that the oxygen content on the surface and subsurface of Cu nanoparticles was the key to achieve high activity and selectivity of hydrocarbons/alcohols, even more important than the existence of the Cu (100) crystal plane. Cu nanoparticles treated by O<sub>2</sub> plasma had lower overpotential and higher selectivity for ethylene, ethanol, and n-propanol, of which the selectivity for ethylene and ethanol was 45% and 22%, and the maximum Faraday efficiency (FE) of C2 and C3 products can reach 73%.

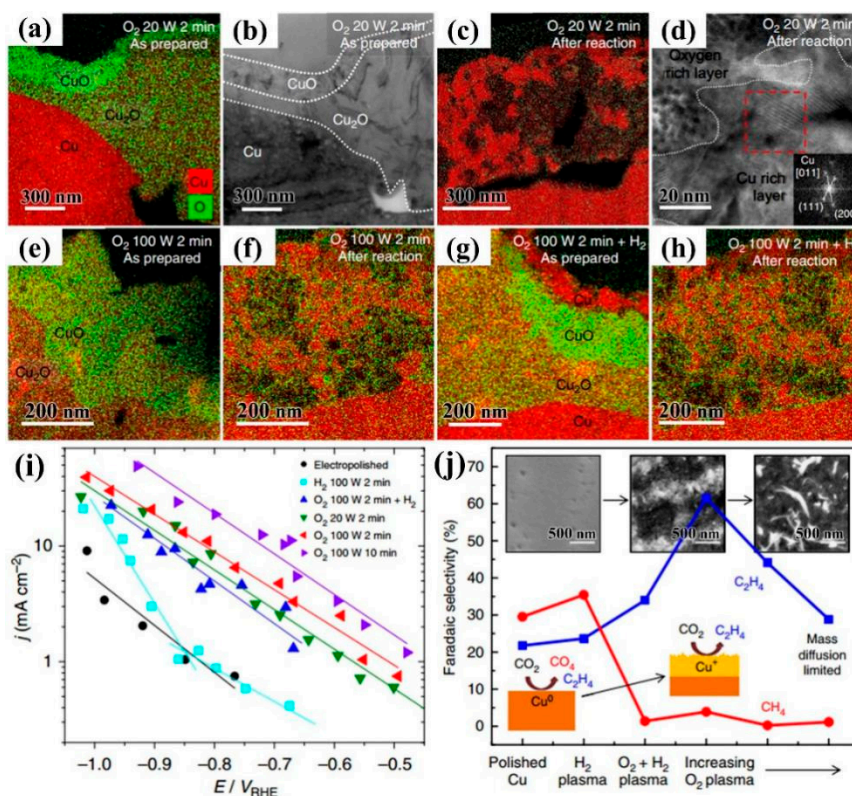


**Figure 8.** (a,c,e–h) EDS images and (b,d) HRTEM images of different plasma activated copper foil before and after reaction; (i) electrochemical activity during CO<sub>2</sub>RR process; (j) hydrocarbon selectivity of plasma treated Cu foil. The corresponding inset SEM images were after the reaction: H<sub>2</sub> plasma treated metal Cu foil, O<sub>2</sub> plasma treated with Cu foil at 20 W for 2 min, and O<sub>2</sub> plasma treated at 100 W for 10 min, respectively [52]. (Reproduced with permission from [52]. Nature Publish Group, 2016).

### 3.2. Transition Metal Oxides

#### 3.2.1. Cobalt Oxides

Cobalt oxide ( $\text{CoO}_x$ ) has attracted much attention for its superior catalytic activity in electrocatalysts [54,55]. In 2017, Kim et al. [56] prepared  $\text{Ag@Co}_3\text{O}_4$  core-shell hybrid nanocrystals in aqueous solution by treating Ag and Co electrode wires with solution plasma technology. Compared with Ag and Ag–Co electrocatalysts prepared in alcohol solution, it showed a better electronic effect and geometric effect, which was beneficial to the fracture of the O–O bond for ORR, resulting in the catalytic activities being 5.2 and 2.6 times higher, respectively. The modification of the carrier can also effectively improve the catalytic activity. Taiwo et al. [57] synthesized three-dimensional nanoporous graphene sheets with highly specific surface areas as a catalyst carrier by microwave-induced plasma, and then doped them with nitrogen and supported  $\text{Co}_3\text{O}_4$  nanoparticles to prepare  $15\text{Co}_3\text{O}_4/\text{N-AP}/800$  electrocatalysts. The catalysts exhibited excellent electrical conductivity and ORR performance, showing that the Tafel slope was 42 mV/dec, which was better than 82 mV/dec of Pt/C. In 2018, Lang et al. [58] used DC arc discharge plasma to synthesize CoO nanospheres mixed with  $\text{La}_2\text{O}_3$  and Pt/C to prepare highly active CO–La–Pt ternary ORR catalysts for Li–O batteries. The specific capacity and energy density of the electrode reached 3250.2 mAh/g and 8574.2 Wh/kg at 0.025 mA/cm<sup>2</sup>, and the capacity retention rate reached 38.3% after 62 cycles.

Transition metal oxides with abundant defects and vacancies were prepared by plasma etching, which exhibited excellent electrocatalytic performance [59]. In 2016, Xu et al. [60] used Ar plasma to treat  $\text{Co}_3\text{O}_4$  nanosheets, which produced oxygen vacancies on the surface of  $\text{Co}_3\text{O}_4$  nanosheets, which had higher current density and lower initial potential than untreated  $\text{Co}_3\text{O}_4$  nanosheets. The catalysts showed good OER performance and the current density was increased by 10 times at a voltage of 1.6 V. Wang et al. [61] introduced oxygen vacancies in cobalt oxyhydroxide ( $\text{CoOOH}$ ) by Ar plasma technique. It was proven by density functional theory that  $\text{V}_0\text{-COOH}$  catalysts with oxygen vacancies could initiate additional reaction steps to accelerate the oxidation of  $\text{H}_2\text{O} \rightarrow \text{H}_2\text{O}^* \leftrightarrow (\text{HO} + \text{H})^*$  and  $(\text{HO} + \text{H})^* \leftrightarrow \text{HO}^* + \text{H}^+ + \text{e}^-$ , and had a lower kinetic barrier. At the same time, the experimental observation confirmed that the two sites could promote the OER catalytic activity of  $\text{V}_0\text{-CoOOH}$ , which accelerated the deprotonation process and enhanced water oxidation due to their synergistic catalysis. Meanwhile, this method can also be extended to other OER catalysts, which has broad application prospects. In 2018, Ma et al. [62] applied  $\text{Co}_3\text{O}_{4-x}$  with oxygen-rich vacancies, treated by Ar plasma, to the catalytic reactions of ORR (half-wave potential 0.84 V) and OER (overpotential of 330 mV and Tafel slope of 58 mV/dec), resulting in excellent catalytic activity, as shown in Figure 9b. The Zn-based hybrid battery (Figure 9a) prepared on this basis can simultaneously carry out two kinds of electrochemical reactions (OER and ORR electrocatalysis, and reversible  $\text{Co-O} \leftrightarrow \text{Co-O-OH}$  redox reaction), with a high power density of 3200 W/kg and a high energy density of 1060 Wh/kg. The battery showed good water resistance and washing resistance. Its capacity retention rate was 99.2% after 20 h of immersion test and 93.2% after 1 h of washing test. More interestingly, when exposed to air from underwater, the battery can automatically restore the power output, with excellent electrochemical performance, good environmental adaptability, and “air recyclability,” so was considered to have potential to become the next generation of energy storage device and be widely used in flexible wearable electronic devices and other technical fields (Figure 9c).

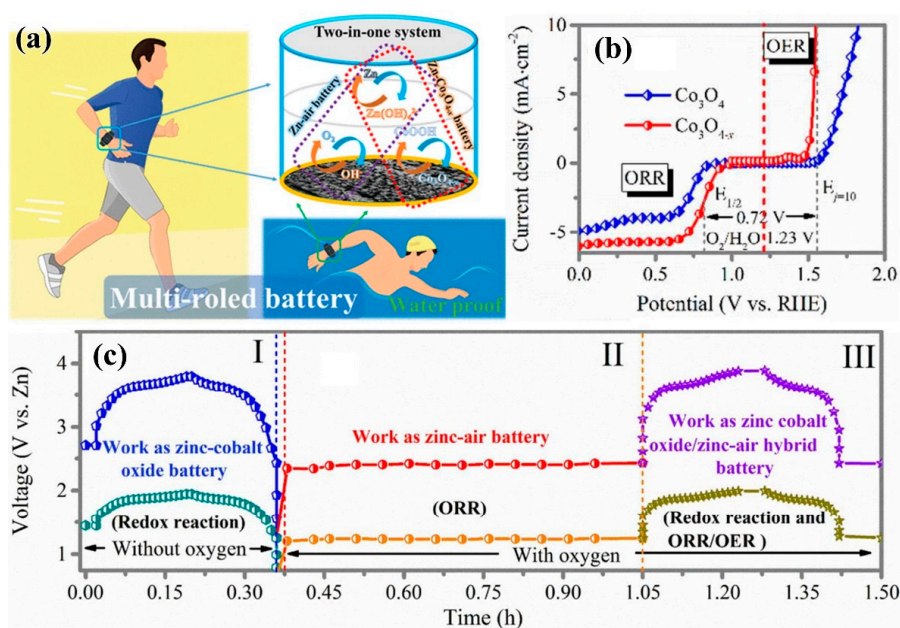


**Figure 9.** (a) The schematic diagram of Zn–Co<sub>3</sub>O<sub>4-x</sub>/Zn-air hybrid battery; (b) the overall polarization curve of Co<sub>3</sub>O<sub>4</sub> nanorods and Co<sub>3</sub>O<sub>4-x</sub>; (c) the constant current charge/discharge curve of Zn–Co<sub>3</sub>O<sub>4-x</sub>/Zn-air hybrid battery. (I) Work of the Zn–Co<sub>3</sub>O<sub>4-x</sub> battery in an anaerobic environment; (II) Work of the zinc-air battery in an aerobic environment; (III) Work of the hybrid battery in an aerobic environment [62]. (Reproduced with permission from [62]. American Chemical Society, 2018).

The doping of heteroatoms can also improve the electrocatalytic activity of CoO<sub>x</sub>, and the plasma technology can be used to dope nitrogen [63]. In 2017, Xu et al. [64] found that surface etching and nitrogen doping were realized on Co<sub>3</sub>O<sub>4</sub> nanosheets by N<sub>2</sub> plasma. The sample N–Co<sub>3</sub>O<sub>4</sub> had more active sites due to N-doping and oxygen vacancies, leading to a significant improvement in electronic conductivity. Compared to Co<sub>3</sub>O<sub>4</sub> nanosheets (1.79 V and 234 mV/dec), it showed a lower potential (1.54 V) at a current density of 10 mA/cm<sup>2</sup> and a Tafel slope of 59 mV/dec. Uhlig et al. [65] directly treated the CoAc/C precursor with N<sub>2</sub> plasma, that simultaneously achieved nitrogen doping of the carrier and active components. The product showed excellent ORR catalytic activity in 0.1 M KOH and 0.1 M K<sub>2</sub>CO<sub>3</sub> solutions. However, cobalt oxide produced more by-products, which may have resulted in membrane damage to the fuel cell, which remains unimproved upon.

Elemental P can be doped into an oxide by plasma [66]. In 2017, Xiao et al. [67] found that P atoms were immediately transported and filled into the position of an oxygen vacancy defect, which was a structural defect caused by surface oxygen etching of materials by Ar plasma airflow treatment (Figure 10a–f). The 3p orbital and 3d orbital of P atoms have lone pair of electrons, so the V<sub>0</sub> of Co<sub>3</sub>O<sub>4</sub> filled with P atoms can be used to effectively stabilize vacancies, which can induce local charge density and adjust surface charge state, and also can be used to adjust the relative proportion of Co<sup>2+</sup>/Co<sup>3+</sup>, improving the adsorption and electrocatalytic properties of materials [68]. As can be seen in Figure 10g–i, V<sub>0</sub>-Co<sub>3</sub>O<sub>4</sub> had a relatively lower coordination number than Co<sub>3</sub>O<sub>4</sub> due to the formation of oxygen vacancies, and P–Co<sub>3</sub>O<sub>4</sub> had a much higher coordination number than V<sub>0</sub>-Co<sub>3</sub>O<sub>4</sub> and Co<sub>3</sub>O<sub>4</sub>, due to the filling of P atoms. When P occupied the vacancy sites, electrons migrated out of the 3d orbital of Co, and more Co<sup>2+</sup> (Td) remained in P–Co<sub>3</sub>O<sub>4</sub>, which exhibited excellent catalytic activity for HER and OER. P–Co<sub>3</sub>O<sub>4</sub> required only an overpotential of 120 mV in the HER process and the overpotential of 280 mV in the OER process at the current density of 10 mA/cm<sup>2</sup>. The Tafel slopes for HER and OER were 52 mV/dec and 51.6 mV/dec, respectively. P–Co<sub>3</sub>O<sub>4</sub> can effectively catalyze full water-splitting in a 5 M KOH solution (80 °C), which showed an overpotential of 420 mV at a current density of 100 mA/cm<sup>2</sup>.

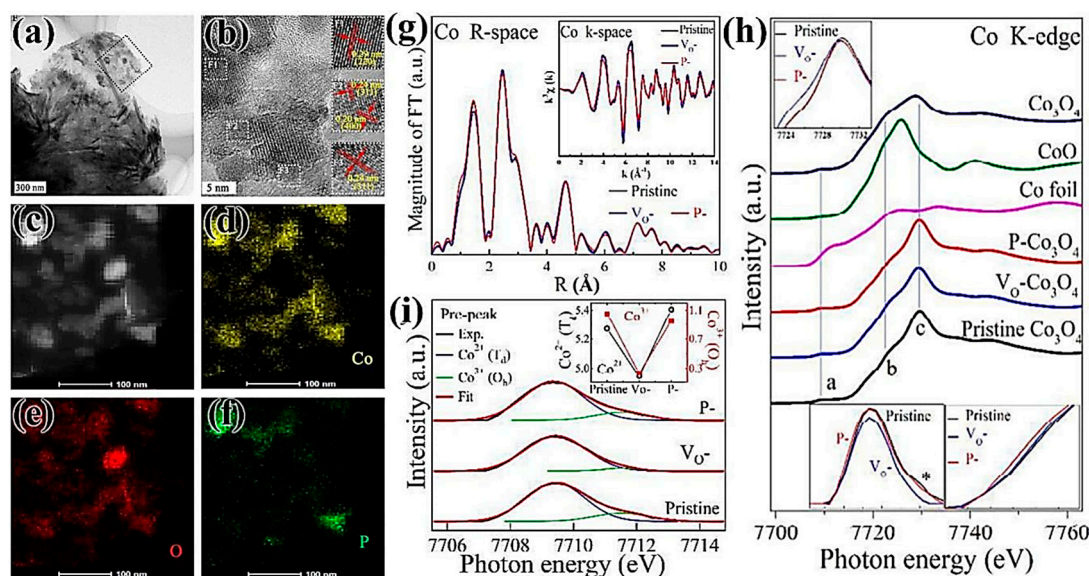


**Figure 10.** (a) TEM images, (b) HRTEM images, and (c–f) STEM-EDX elemental mapping images of P-Co<sub>3</sub>O<sub>4</sub>; (g) Co K-side extended x-ray absorption fine structure (EXAFS). The inset is the Fourier-transformed EXAFS oscillations; (h) Co K-edge XANES spectra of pristine V<sub>0</sub>-Co<sub>3</sub>O<sub>4</sub> and P-Co<sub>3</sub>O<sub>4</sub>. Top inset magnifies the main peak region. Bottom insets magnify the pre-peak region; (i) deconvoluted pre-peak of Co K-edge XANES. Inset compares the amount of Co<sup>2+</sup>(Td) and Co<sup>3+</sup>(Oh) states of pristine, V<sub>0</sub>-Co<sub>3</sub>O<sub>4</sub>, and P-Co<sub>3</sub>O<sub>4</sub> [67]. (Reproduced with permission from [67]. Royal Society of Chemistry, 2017).

In addition, excellent electrocatalytic performance can be obtained by reducing the size of the catalysts to expose more active sites. Dou et al. [69] prepared atomic-scale CoO<sub>x</sub>-ZIF (Zeolitic Imidazolate Framework, ZIF) catalysts by directly treating ZIF-67 precursors with O<sub>2</sub> plasma. ZIF-67 has an abundant pore structure, which provided abundant channels for O<sub>2</sub> to enter ZIF to activate Co<sup>2+</sup> to obtain atomic-scale CoO<sub>x</sub>. After treatment with O<sub>2</sub> plasma, the porous structure and large surface area of ZIF-67 were still retained, which were very conducive to the transport of materials toward OER. The prepared atomic-scale CoO<sub>x</sub>-ZIF catalysts can provide abundant active sites for oxygen evolution reaction, and its catalytic performance for OER was better than that of noble metal catalyst RuO<sub>2</sub>. The atomic scale electrocatalysts were obtained directly in-situ in MOFs (metal organic frameworks, MOFs) by that method for the first time, which provided a new idea for the convenient preparation of atomic scale electrocatalysts.

### 3.2.2. Perovskite-Type Oxides

Perovskite-type oxide ABO<sub>3</sub> is a new type of inorganic nonmetallic material with unique physical and chemical properties. A-site is usually the ion of a rare earth or alkaline earth element, and B-site is the ion of transition element. A-site and B-site can be partially replaced by other metal ions with similar radii and keep their crystal structures unchanged. Therefore, ABO<sub>3</sub> is an ideal sample for studying the surface and catalytic performance of catalysts in theory, which has great development potential in the fields of environmental protection and industrial catalysis [70]. In particular, unlike the anion vacancies in other metal oxides, ABO<sub>3</sub> can also achieve cation vacancies. Chen et al. [71] used Ar plasma technology to surface-treat the SnCo<sub>0.9</sub>Fe<sub>0.1</sub>(OH)<sub>6</sub> (SnCoFe) precursor and adjusted the electrocatalytic activity of OER by defect engineering. Because Sn(OH)<sub>4</sub> had weak chemical bonds and its lattice energy was much lower than that of cobalt or iron hydroxides, Sn vacancies preferentially formed in the process of forming various cationic vacancies, thus a perovskite-type hydroxide (SnCoFe–Ar) electrocatalyst with rich Sn vacancies has been developed. The abundant Sn vacancies made the catalyst materials have a larger specific surface area and superhydrophilicity, exposed more CoFe active

sites, and created more 1–2 nm channels on the surfaces of the catalyst materials, which improved the material transport capacity and electronic transport capacity, and optimized the adsorption capacity of the reactants. Compared with the overpotential of 420 mV and Tafel slope of 77.0 mV/dec for SnCoFe, the overpotential and the Tafel slope of the SnCoFe–Ar were 300 mV and 42.3 mV/dec at the current density of 10 mA/cm<sup>2</sup>, which exhibited superior catalytic performance for OER.

Transition metal ions also affect the catalytic performance of the electrocatalysts. Hayden et al. [72] successfully prepared SrTi<sub>1-x</sub>Fe<sub>x</sub>O<sub>3-y</sub> (STFO) perovskite-type composite gradient electrocatalysts by high-throughput physical vapor deposition (HT-PVD) with O<sub>2</sub> plasma. With the increase of x value, the lattice parameters of STFO increased from 0.392 + 0.001 nm of SrTiO<sub>3</sub> to 0.386 + 0.001 nm of SrFeO<sub>3</sub>, and the conductivity increased as well. When x > 0.75, the conductivity reached  $\rho = 0.041$  S/cm. The corresponding OER reduced the initial potential at current 100  $\mu$ A from 1.52 VRHE (x = 0.2) to 1.40 VRHE (x = 0.85), but the high OER activity was accompanied with low stability. Therefore, SrTi<sub>0.5</sub>Fe<sub>0.5</sub>O<sub>3-y</sub> showed the best ORR activity and electrode stability.

In order to develop efficient electrocatalysts with extraordinary mass activity and stability, Chen et al. [73] deposited amorphous SrCo<sub>0.85</sub>Fe<sub>0.1</sub>Po<sub>0.05</sub>O<sub>3- $\delta$</sub>  (SCFP) nano-thin films with weak chemical bonds on the conductive nickel foam (NF) substrate by high-energy Ar plasma. The rapidly reconstituted SCFP-NF bifunctional catalyst exhibited good electron conductivity, ultra-high activity, and stability, due to the destruction of strong chemical bonds by plasma in the crystalline SCFP target. The ultra-high quality activity (overpotential 550 mV) of 1000 mA/mg in 1.0 M KOH solution was about 2.1 times higher than that of RuO<sub>x</sub>-NF coupled Pt-NF electrode, as shown in Figure 11a,b. At the same time, the catalysts exhibited outstanding catalytic activity with a water decomposition stability of 650 h (current density of 10 mA/cm<sup>2</sup>), which was significantly superior to the current RuO<sub>x</sub>-NF coupled Pt-NF electrode, as shown in Figure 11c–e. The simple reconstruction strategy was expected to be used in other advanced energy conversion and storage devices to develop new and efficient catalysts.

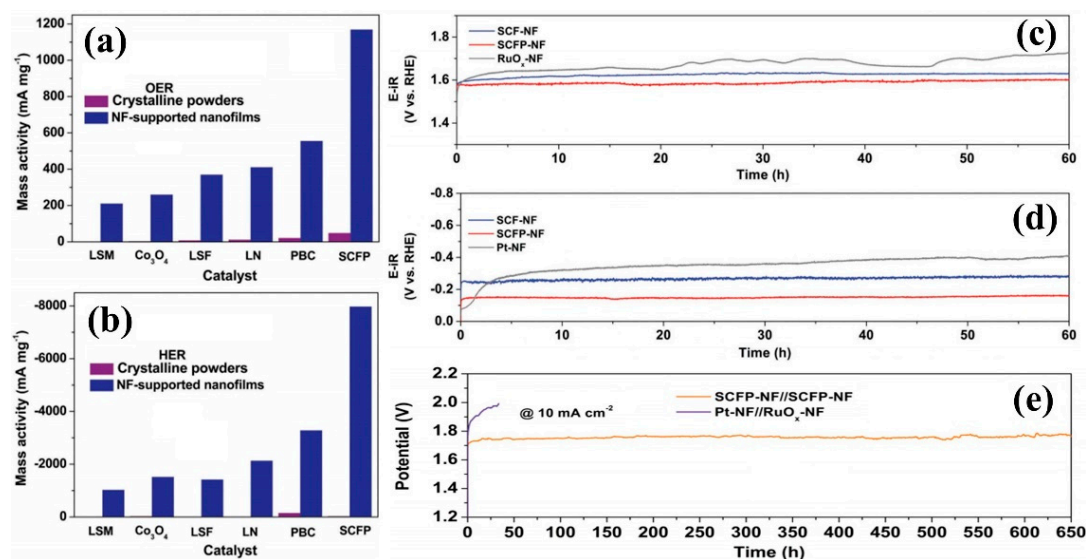


**Figure 11.** Comparison of the mass activity at an overpotential of 0.35 V between crystalline powders and NF-supported nanofilms for the oxygen evolution reaction (OER) (a) and hydrogen evolution reaction (HER) (b); the stability tests of SCFP-nickel foam (NF) and control samples for OER (c) and HER (d); (e) The stability tests for the water splitting of bifunctional SCFP-NF catalysts and Pt-NF coupled RuO<sub>x</sub>-NF [73]. (Reproduced with permission from [73]. Wiley-VCH, 2018).

### 3.2.3. Two-Dimensional (2D) Layered Double Hydroxides

Transition-metal layered double hydroxides (LDH) have unique 2D structures, large specific surface areas and special electronic structures, showing good electrocatalytic performance [74,75]. The LDHs prepared by the conventional methods have a high number of layers, which limits the exposure of the electrocatalytic active sites, and thus inhibits the electrocatalytic activity. At present, the method of liquid phase exfoliation to prepare LDHs generally uses organic solvents, which has the disadvantages of substantial time-consumption, toxicity, and easy adsorption of organic solvents. Compared with traditional liquid phase exfoliation, plasma exfoliation has the advantages of cleanliness, rapidity, and efficiency, and avoids the adsorption of organic solvent molecules. In 2017, Liu et al. [76] prepared 2D ultra-thin nanosheets (CoFe-LDHs–H<sub>2</sub>O) by treating bulk CoFe bimetallic hydroxide nanosheets (CoFe-LDHs) with water plasma technology, which can be stabilized in the form of powder, as shown in Figure 12a,b. Compared with bulk CoFe-LDHs, the thickness of CoFe-LDHs–H<sub>2</sub>O nanosheets decreased significantly (Figure 12c,g), and the 2D base surface became rough (Figure 12d,h). From Figure 12e,f,i,j, it can be seen that water plasma had a very good peeling effect on CoFe-LDHs nanosheets, as the thickness of nanosheets decreased from 25.2 nm to 1.54 nm. The obtained CoFe-LDHs–H<sub>2</sub>O had larger specific surface area, resulting in many cobalt vacancies, iron vacancies, and oxygen vacancies on its surface, which enhanced the adsorption of OER intermediates and further boosted the catalytic activity. Tafel slope and charge transfer impedance decreased significantly, such that the overpotential potential was only 36 mV/dec.

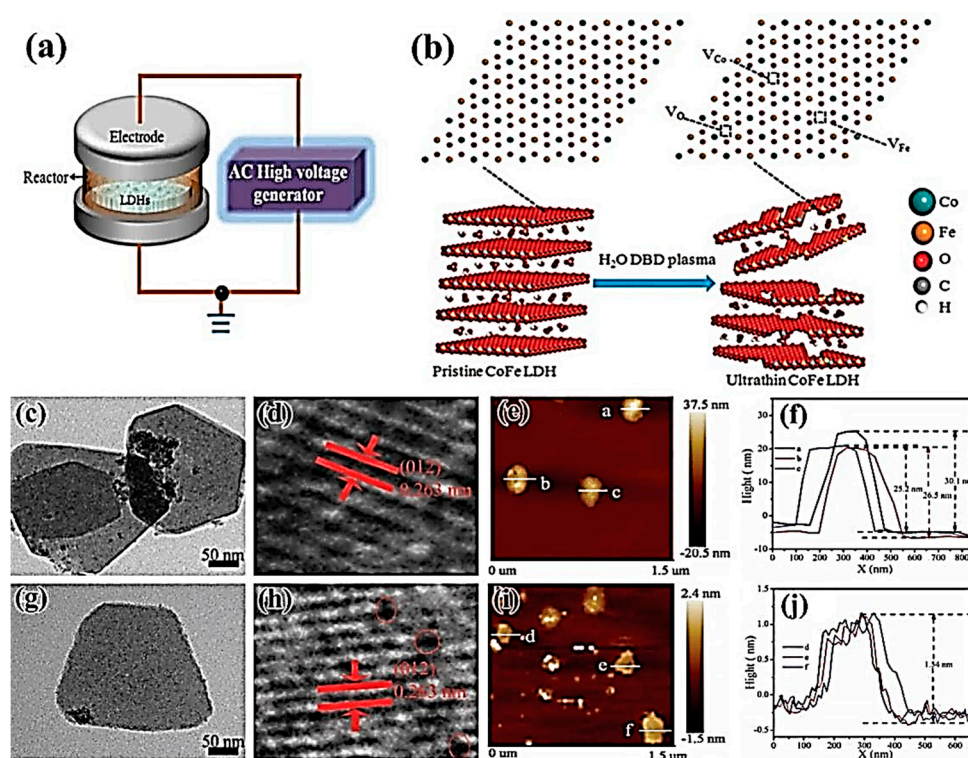


**Figure 12.** The schematic diagram of (a) a dielectric barrier discharge (DBD) reactor and (b) water DBD plasma-activated stripping of CoFe-LDHs nanosheets; TEM, HRTEM, and atomic force microscope (AFM) images and corresponding nanosheet thickness images of bulk CoFe-LDHs (c–f) and plasma-treated CoFe-LDHs–H<sub>2</sub>O samples (g–j) [74]. (Reproduced with permission from [74]. Royal Society of Chemistry, 2017).

In the meantime, Wang et al. [77,78] obtained 2D ultra-thin CoFe-LDHs–Ar and CoFe-LDHs–N<sub>2</sub> nanosheets by treating CoFe-LDHs with Ar plasma and N<sub>2</sub> plasma, respectively. Gas plasma technology was not only non-toxic, clean and time-saving, but CoFe-LDHs–Ar and CoFe-LDHs–N<sub>2</sub>

exfoliated by the dry method also had abundant oxygen vacancies, cobalt vacancies, and iron vacancies. The formation of multiple vacancies was conducive to regulating the electronic structure of the material surface, reducing the coordination number around cobalt and iron atoms, increasing the degree of chaos around atoms, and facilitating the adsorption of the oxygen evolution reaction intermediate, which led to improving the electrocatalytic performance of the material. CoFe-LDHs–Ar nanosheets exfoliated by Ar plasma exhibited good oxygen precipitation performance. The overpotential of CoFe-LDHs–Ar nanosheets was only 266 mV at the current density of 10 mA/cm<sup>2</sup>, showing good activity. CoFe-LDHs–N<sub>2</sub> nanosheets stripped by N<sub>2</sub> plasma not only had abundant metal vacancies and oxygen vacancies, but also realized nitrogen doping. The doping of elemental nitrogen was beneficial to changing the electronic structure around the reaction site and improving the catalytic activity by adsorbing oxygen precipitation intermediates, and the resulting defect-rich 2D ultra-thin CoFe-LDHs–N<sub>2</sub> nanosheets made it easy to expose more electrocatalytic active sites to increase their oxygen evolution performance. The overpotential was only 233 mV at the current density of 10 mA/cm<sup>2</sup>, and the Tafel slope and charge transfer impedance were also reduced, which had very good stability. The new method of stripping 2D layered materials to achieve nitrogen doping and defect-richness simultaneously can be used for reference to other similar materials.

### 3.2.4. Other Metal Oxides

In addition, other transition metal oxides are also used as electrocatalysts. For example, in 2017, Oturan et al. [79] prepared sub-stoichiometric titanium oxide (Ti<sub>4</sub>O<sub>7</sub>) by plasma deposition and electrocatalytic oxidation to treat the pollutant antibiotic amoxicillin (AMX), which can rapidly oxidize and degrade 0.1 mM (36.5 mg/L) AMX in a short time. Luo et al. [80] prepared FeO<sub>x</sub>/C electrocatalysts by uniformly depositing iron oxide clusters on porous carbon substrates with high ionized iron plasma generated by arc discharge. It was found that the catalysts showed good ORR and OER properties, and an excellent rate performance and cycle life in a Li–O<sub>2</sub> battery. A discharge capacity of 500 mAh/g was retained after 37 cycles at the current density of 100 mA/cm<sup>2</sup>. In 2018, Peng et al. [81] prepared MnO<sub>x</sub>@C-D electrocatalysts by dielectric barrier discharge technology for ORR. Because of the effect of plasma, the catalysts allowed manganese ions with different valences to coexist, and had high oxygen adsorption capacities. The aggregation of nanometer catalysts was inhibited at a medium temperature, which showed a higher reaction activity than that of the catalysts prepared by traditional calcination method. Jiang et al. [82] induced abundant defects on the surface of MnO<sub>2</sub> nanowires by Ar plasma etching, and observed that Ar–MnO<sub>2</sub> had abundant edges and oxygen vacancies to produce more active sites, showing excellent ORR performance. At the current density of 157 mA/cm<sup>2</sup>, the power density of Al–air battery based on A–MnO<sub>2</sub> catalysts can reach 159 mW/cm<sup>2</sup>, which is much higher than that of untreated MnO<sub>2</sub> catalysts (115 mW/cm<sup>2</sup>).

In the process of HER catalysis, pre-reduction of transition metal oxides is an effective way to improve the catalytic activity of HER. Zhang et al. [83] treated NiMoO<sub>4</sub> nanowire arrays by carbon plasma for 30 s, which formed Ni<sub>4</sub>Mo nanoclusters on the surface and deposited a layer of graphitized carbon, as shown in Figure 13a–d. Compared with NiMoO<sub>4</sub> nanowire arrays treated by H<sub>2</sub> reduction, the sample (C-60s) exhibited excellent catalytic activity for hydrogen evolution (Figure 13e–g), and could maintain its array morphology, chemical composition, and catalytic activity during long-term intermittent hydrogen evolution. It opened up a new way for simultaneous activation and stabilization of transition metal oxide electrocatalysts. In 2018, Geng et al. [84] used H<sub>2</sub> plasma to surface-treatment of 2D ZnO nanosheets, which produced abundant oxygen vacancy defects on the surface. Although these oxygen vacancy defects did not increase the number of active centers, they can lead to the efficient activation of CO<sub>2</sub> molecules in the electron-rich state and enhance the electrochemical catalytic reduction activity of CO<sub>2</sub>. At the voltage of –1.1 V compared to RHE, the oxygen-rich ZnO nanosheets with vacancies can effectively reduce the CO<sub>2</sub> to a CO product with a current density of –16.1 mA/cm<sup>2</sup> and a Faraday efficiency of about 83%, exhibiting excellent catalytic activity for CO<sub>2</sub>RR.



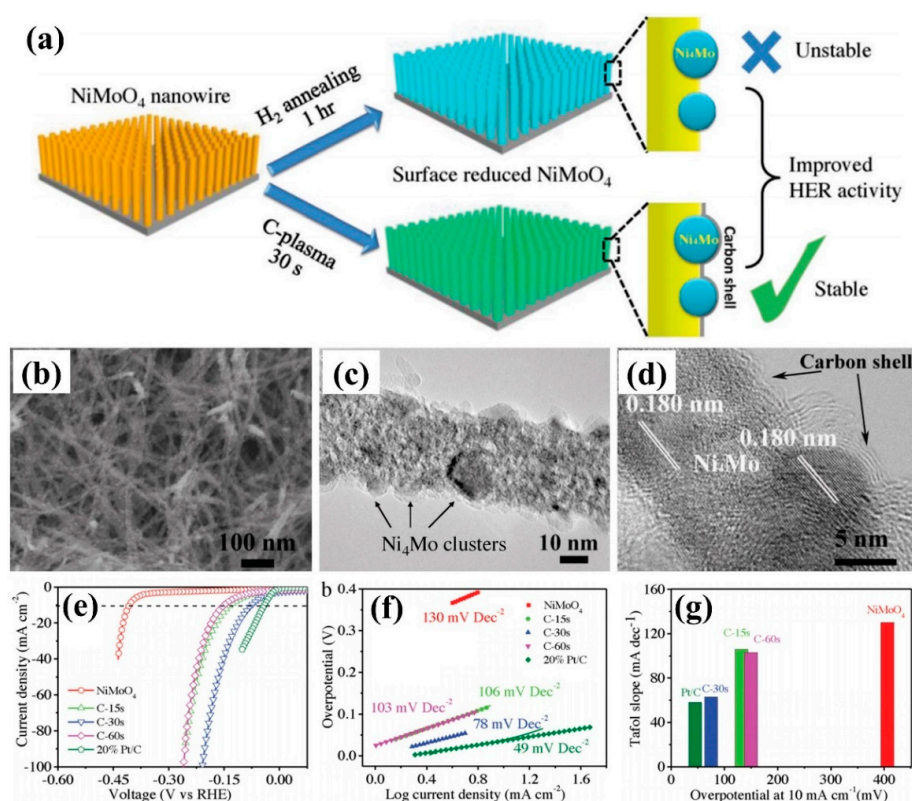


**Figure 13.** (a) The preparation of C-plasma treated and H<sub>2</sub> annealed NiMoO<sub>4</sub>; (b) SEM and (c,d) TEM images of the sample C-30s; the electrochemical performance tests of the sample: (e) linear sweep voltammetry (LSV) curve, (f) Tafel slope, and (g) the relationship between overpotential and Tafel slope at current density of 10 mA/s [83]. (Reproduced with permission from [83]. Wiley-VCH, 2018).

### 3.3. Transition Metal Sulfides

Transition metal sulfides which have received extensive attention in recent years, have become new and highly efficient electrocatalysts, particularly HER catalysts. The hydrogen evolution reaction mainly occurs at the boundary of 2D materials in which the atom is incompletely coordinated. Therefore, the preparation of 2D transition metal sulfides with incompletely coordinated atomic boundaries is the key to whether the material can replace the noble metal platinum. Li et al. [85] etched 2D TaS<sub>2</sub> nanosheets by using O<sub>2</sub> plasma technology. It was found that the plasma could control the processing of high-density atomic-scale pores on three-dimensional (3D) two-layer crystals, which can increase the catalytic sites and effectively improve the hydrogen evolution catalytic activity of 2D materials, as shown in Figure 14a. As can be seen from Figure 14b–g, the atomic defect density increased with the increase of processing time, which exhibited excellent HER catalytic activity of treatment at 15 min.

2D MoS<sub>2</sub> is also used for electrocatalytic reactions, which can also be used to enhance the activity by Ar, O<sub>2</sub>, and H<sub>2</sub> plasma. Tao et al. [86] prepared Ar–MoS<sub>2</sub> and O<sub>2</sub>–MoS<sub>2</sub> thin film materials for OER catalytic reaction using Ar and O<sub>2</sub> plasma treatment, respectively. The hydrophilic contact angles of Ar and O<sub>2</sub>–MoS<sub>2</sub> were found to be 61.8° and 48.4°, which were significantly better than untreated MoS<sub>2</sub> (96.5°). The Tafel slope of O<sub>2</sub>–MoS<sub>2</sub> was up to 105 mV/dec, which was significantly better than Ar–MoS<sub>2</sub> (117 mV/dec) and MoS<sub>2</sub> (160 mV/dec). In 2018, Zhang et al. [87] and Huang et al. [88] found that MoO<sub>3</sub> species were formed at the edge and plane positions of MoS<sub>2</sub> by using O<sub>2</sub> plasma to treat MoS<sub>2</sub> and H<sub>3</sub>Mo<sub>12</sub>O<sub>40</sub>P/MoS<sub>2</sub> composite intercalation compounds respectively. The MoO<sub>3</sub> can also be reduced and decomposed from the lattice of MoS<sub>2</sub> in the HER catalytic process, effectively improving the HER catalytic activity of MoS<sub>2</sub>. In addition, the presence of S defects also enhanced the catalytic activity of MoS<sub>2</sub> for HER. Cheng et al. [89] treated MoS<sub>2</sub> with H<sub>2</sub> plasma, and the sample MoS<sub>2</sub> treated for 15 min produced high density S vacancies on the base plane of single-layer crystalline

MoS<sub>2</sub>, whose overpotential could reach 240 mV (versus RHE) at the current density of 10 mA/cm<sup>2</sup>. The amorphous a-MoS<sub>2</sub> treated by H<sub>2</sub> plasma had abundant sulfur vacancies, resulting in a decrease of overpotential from 206 mV of a-MoS<sub>2</sub> to 143 mV of MoS<sub>1.7</sub> [90].

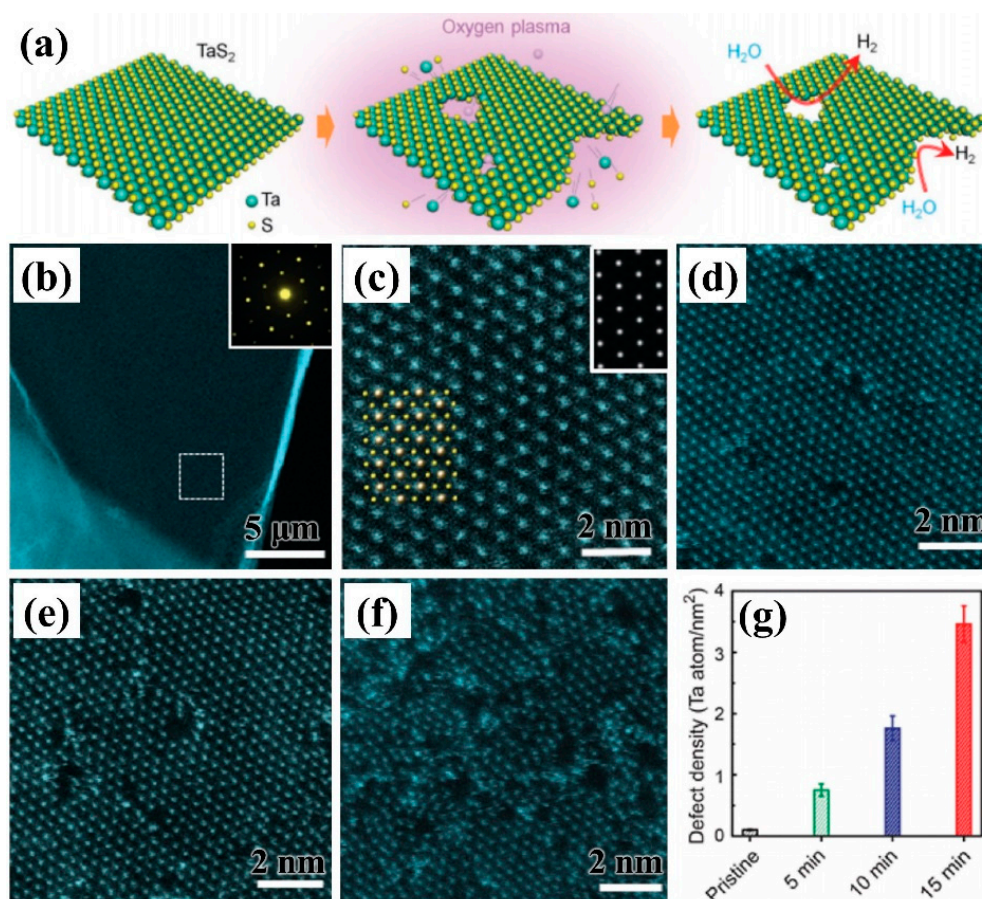


**Figure 14.** (a) Mechanism diagram of O<sub>2</sub> plasma treated TaS<sub>2</sub> nanosheets for HER; (b) TEM images and (c) HAADF-STEM images of TaS<sub>2</sub>; (d–f) HAADF-STEM images by plasma treatment for 5 min, 10 min, and 15 min; (g) the density of edge Ta atoms [85]. (Reproduced with permission from [85]. Wiley-VCH, 2016).

Cobalt sulfide also has good electrocatalytic activity. Dou et al. [91] prepared bifunctional catalysts with catalytic ORR and OER by simultaneously etching and doping the catalyst's surface and using NH<sub>3</sub> plasma. Co<sub>9</sub>S<sub>8</sub> nanoparticles (Co<sub>9</sub>S<sub>8</sub>/G) loaded on graphene were treated by ammonia plasma. Nitrogen was successfully doped into the lattices of Co<sub>9</sub>S<sub>8</sub> and graphene by the treatment of Co<sub>9</sub>S<sub>8</sub> nanoparticles loaded on graphene (Co<sub>9</sub>S<sub>8</sub>/G) with NH<sub>3</sub> plasma. Moreover, partial etching also occurred on the surface of Co<sub>9</sub>S<sub>8</sub> and graphene. The doping of heteroatoms can effectively adjust the electronic structure of Co<sub>9</sub>S<sub>8</sub> and graphene, while the etching of the surface can expose the catalysts to more catalytically active sites, which can obtain a high activity bifunctional electrocatalysts with similar ORR catalytic performance to commercial Pt/C, and OER catalytic performance superior to RuO<sub>2</sub>. In 2018, Zhang et al. [92] prepared a sulfur-rich, Co<sub>3</sub>S<sub>4</sub>, ultrathin porous nanosheet with abundant sulfur vacancies (Co<sub>3</sub>S<sub>4</sub> PNS<sub>vac</sub>) using Ar plasma to treat the Co<sub>3</sub>S<sub>4</sub>/TETA precursor. When the hydrogen evolution potential was 200 mV, the mass activity was as high as 1056.6 A/g, which is 107 and 14 times that of Co<sub>3</sub>S<sub>4</sub> nanoparticles and nanosheets respectively, which was also better than the HER electrocatalytic activity of Pt/C. In addition, the simple and rapid chemical conversion strategy can be extended to the synthesis of ultra-thin porous CoSe<sub>2</sub> and NiSe<sub>2</sub> sheets with anion-rich defects,

due to their universality, which opened up new ways to control the electrocatalytic performance of 2D nanomaterials through defect engineering and ultra-thin porous structure engineering.

In recent years, self-supporting electrode materials have attracted widespread attention. In 2018, He et al. [93] synthesized CuI nanosheet arrays by using dielectric barrier discharge (DBD) plasma with iodine vapor on copper foam, and then prepared Cu<sub>2</sub>S nanosheet arrays via sulfur ion exchange. The Cu<sub>2</sub>S/CF showed excellent OER catalytic activity in 1 M KOH solution with an overpotential of only 290 mV at the current density of 10 mA/cm<sup>2</sup>. Yeo et al. [94] used a PEALD technique to grow a tungsten disulfide (WS<sub>2</sub>) film on a Ni mesh (WS<sub>2</sub>/Ni-foam), which exhibited superior HER activity. In acidic electrolyte, the overpotential and the Tafel slope of the catalysts were 280 mV and 63 mV/dec at a high working current density of 100 mA/cm<sup>2</sup>. Daniel et al. [95] modified WS<sub>2</sub> and MoS<sub>2</sub> by SF<sub>6</sub>/C<sub>4</sub>F<sub>8</sub> plasma. It was found that their overpotentials shifted to 100 mV and 200 mV, and the Tafel slopes decreased by 50 mV/dec and 120 mV/dec, respectively. Especially for WS<sub>2</sub> samples treated by plasma for 31s, the Tafel slope was only 81 mV/dec. Plasma can also be used to treat the carrier. Qu et al. [96] used a plasma-treated Ni–Fe foam (PNFF) carrier to form a PNFF with many micro-grooves on the surface. Then, CoS/Ni<sub>3</sub>S<sub>2</sub>–FeS nanoflowers were formed by vulcanization, after Co nanoparticles were deposited on PNFF carrier by electrodeposition, which showed the overpotentials toward HER and OER of 75 mV and 136 mV at the current density of 10 mA/cm<sup>2</sup>, respectively. The amount of H<sub>2</sub> and O<sub>2</sub> produced were 680 μmol/h and 1230 μmol/h, respectively, showing high electrocatalytic activity and overall water splitting performance.

### 3.4. Transition Metal Selenides

Transition metal selenides also exhibit excellent electrocatalytic performance, especially for the HER catalytic reaction. [97] HER has become the bottleneck of hydrogen production from electrolytic water due to the slow reaction kinetics. The lower overpotential and the Tafel slope identify the benefits of HER catalytic activity; plus the HER can react at a lower applied voltage. For example, the Tafel slope of a Pt-based catalysts can be reached 30 mV/dec, which is close to the theoretical limit of 29 mV/dec, but its reserves and price limit wider applications. In 2017, Deng et al. [98] used a 3D porous vertical graphene array (VG) prepared by MPECVD as a conductive substrate, and prepared a MoSe<sub>2</sub>/VG/array by hydrothermal method treated by ammonia gas heat treatment modification. Next, the 2H to 1T (2H-1T) phase transition of MoSe<sub>2</sub> was initiated by N doping to form N–MoSe<sub>2</sub>/VG having a 2H-1T composite phase. The introduction of 1T phase reduced the band width of MoSe<sub>2</sub> and improved the electron transport performance. At the same time, N doping increased the hydrogen evolution active site at the edge of MoSe<sub>2</sub> sheet, which showed that the Tafel slope can reach 49 mV/dec, demonstrating a good hydrogen evolution performance. Qu et al. [99] used the glancing angle deposition (GLAD) method combined with the N<sub>2</sub>/H<sub>2</sub> plasma technology to prepare the MoSe<sub>2</sub>/Mo composite, as shown in Figure 15. The plasma-assisted selenization process gave MoSe<sub>2</sub>/Mo a large surface area, while accelerating the charge transfer of the metal phase of MoS<sub>2</sub> exposed to the edge. The Tafel slope of catalysts can reach 34.7 mV/dec, which exhibits excellent HER catalytic activity.

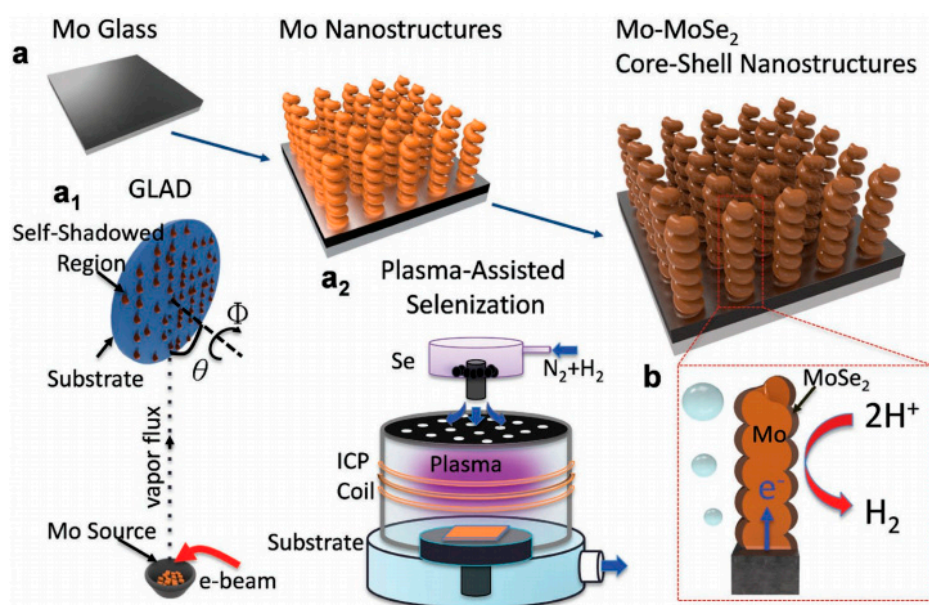


**Figure 15.** (a) Plasma-assisted selenization process: inset of (a1) MoSe<sub>2</sub>/Mo composite prepared by GLAD method; inset of (a2) plasma-assisted selenization treatment. (b) Schematic diagram of HER and charge transfer [99]. (Reproduced with permission from [99]. Wiley-VCH, 2016).

### 3.5. Transition Metal Nitrides

Transition metal nitrides are often used as electrocatalysts, known as “quasi-platinum catalysts,” providing a new way to prepare economical and efficient electrocatalysts. Zhang et al. [100] prepared a three-dimensional porous NiMoN material on carbon cloth with N<sub>2</sub> plasma treatment technology, which displayed high roughness and electron transport capability. The overpotential can reach 109 mV at a current density of 10 mA/cm<sup>2</sup> due to its excellent synergistic effects from Ni, Mo, and N for HER performance. Ouyang et al. [101] used N<sub>2</sub> plasma treatment to grow a 3D structure of nitriding (hNi<sub>3</sub>N) on Ni foam (NF), which showed excellent OER catalytic activity and laid the foundation for the development of a high-performance, metal nitride, energy storage switching electrode. In 2018, Liu et al. [102] produced nickel nitride (Ni<sub>3</sub>N<sub>1-x</sub>) rich in nitrogen vacancies by nitriding Ni foam (NF) by microwave plasma-generation (Figure 16a,b). The presence of nitrogen vacancies effectively promoted the adsorption of water molecules, improved the adsorption-desorption behavior of the intermediate adsorbed hydrogen, and enhanced the HER activity of Ni<sub>3</sub>N<sub>1-x</sub>, as shown in Figure 16c–f. The self-supporting Ni<sub>3</sub>N<sub>1-x</sub>/NF electrode showed an overpotential of 55 mV and a Tafel slope of 54 mV/dec in an alkaline solution at the current density of 10 mA/cm<sup>2</sup>.

Some nitride also exhibits excellent electrocatalytic properties in terms of ORR catalytic performance. Wang et al. [103] deposited high-density discrete Cu<sub>3</sub>N nanocrystals on XC-72 carbon black by plasma enhanced atomic layer deposition (PEALD). It was found that the work function of Cu<sub>3</sub>N nanocrystals was 5.04 eV, which was lower than Pt (5.60 eV). Cu<sub>3</sub>N had stronger electron transfer performance than typical Pt catalysts. At the same time, the synergistic coupling effect between Cu<sub>3</sub>N nanocrystals and carbon support made the Cu<sub>3</sub>N<sub>200</sub>/C sample exhibit a smaller  $\pi$  (= 4.34 eV) than the pure Cu<sub>3</sub>N nanocrystals. It displayed excellent ORR catalytic activity, significantly improved quality activity, and greater durability. Panomsuwan et al. [104] prepared iron-nitrogen-doped carbon nanoparticle–carbon fiber (Fe–N–CNP–CNF) by solution plasma. Because of the synergistic effect of the high graphitization of CNF, the mesoporous/macroporous CNP, the catalytic active center of ORR (graphite N and Fe–N bond), and the carbon-encapsulated Fe/Fe<sub>3</sub>C particles, the Fe–N–CNP–CNF obtained showed excellent catalytic activity, durability and methanol resistance toward oxygen reduction (ORR) in an alkaline solution. Zhong et al. [105] found that the use of air plasma etching of iron-nitrogen co-doped porous carbon (Fe–N/C) electrocatalysts can remove sp<sup>3</sup> Cs with poor stability

and amorphous  $sp^2$  Cs, exposing more active catalytic  $FeN_4$  centers, and transforming a small number of Fe-based nanoparticles into  $FeN_4$  species, which significantly improved the catalytic activity of Fe–N/C for the oxygen reduction reaction (ORR) in acidic and alkaline electrolytes.

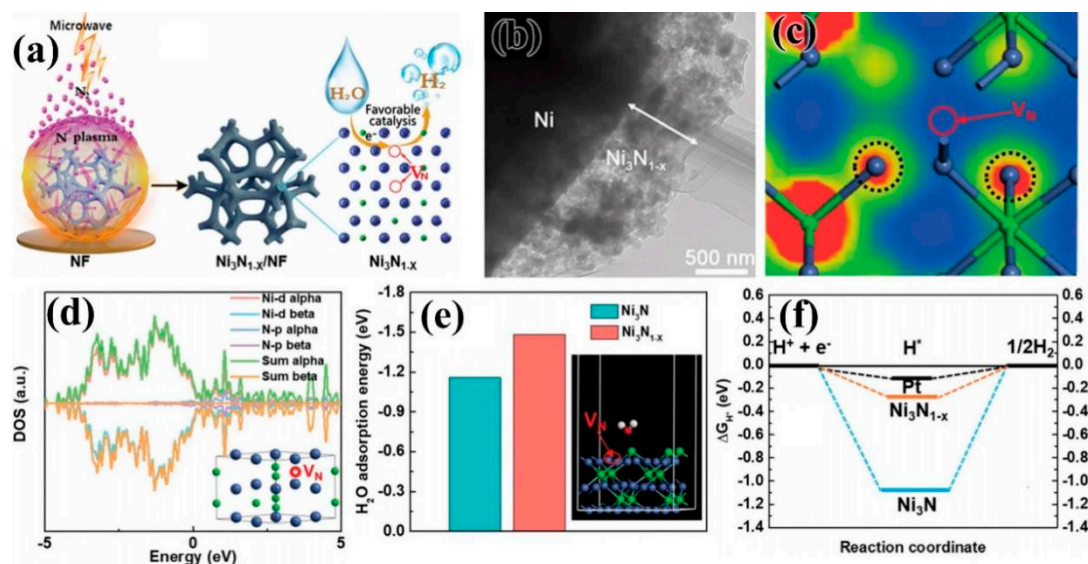


**Figure 16.** (a) Schematic diagram of preparation of self-supporting  $Ni_3N_{1-x}/NF$  electrode by microwave plasma-generation; (b) TEM images, (c) charge density distribution, and (d) the total electron density and partial electron density (TDOS and PDOS) of  $Ni_3N_{1-x}/NF$ ; (e) adsorption energy of  $H_2O$  molecules on the surface of  $Ni_3N$  and  $Ni_3N_{1-x}$ ; (f) free energy of H adsorption by various substances at equilibrium potential [102] (open access).

### 3.6. Transition Metal Phosphides

Transition metal phosphides have attracted great interest as electrocatalytic catalysts, particularly for HER and OER catalysts for electrocatalytic water splitting [106]. Currently, bimetallic phosphides exhibit higher catalytic activity than monometallic compounds [107]. Liang et al. [108] realized the transition of  $NiCo-OH$  to  $NiCoP$  on nickel foam by  $PH_3$  plasma, and prepared  $NiCoP$  electrocatalysts, as shown in Figure 17a, which exhibited excellent HER and OER electrocatalytic activity under alkaline conditions (Figure 17b–d). Zhang et al. [109] used plasma-enhanced chemical vapor deposition (PECVD) to form phosphate and phosphide groups on foamed nickel in the presence of  $PH_3$ ,  $CO_2$ , and  $H_2$  to form  $NiFePi/P$ . The change in the surrounding electronic environment of metal ions, due to the strong synergistic effect between phosphate and phosphide, not only increased the active center, but also improved the wettability and metal properties of the catalyst, the high conductivity, the wettability, and the active sites, which lead to excellent OER performance in an alkaline solution.

The doping of metal elements can also effectively balance the adsorption/desorption of oxygen and hydrogen-containing intermediates of metal phosphides, while enhancing density of electronic states' (DOS) strength and enhancing charge transfer kinetics. Dinh et al. [110] etched metal V-doped  $Ni_2P$  nanosheets ( $V-Ni_2P$ ) by  $O_2$  plasma, and found that V substitution in the prepared  $OV-Ni_2P$  may introduce defects and crystal dislocations, thus increasing the number of active sites and the carrier concentration. The strength of the oxygen bonding and the charge transfer kinetics were significantly enhanced after vanadium doping. Due to the  $O_2$  plasma treatment, the phosphide surface was partially oxidized to produce a phosphate–phosphide region which balanced the adsorption/desorption of hydrogen and oxygen-containing intermediates. After the plasma, the Brunauer-Emmett-Teller (BET) surface area and the hydrophilicity of the material increased significantly.  $O-V-Ni_2P$  had a large surface area ( $168.2 \text{ m}^2/\text{g}$ ) and excellent hydrophilicity (contact angle of  $16.8^\circ$ ), leading to a higher electroactive surface area and a lower charge transfer resistance. The study found that the 10% V-doped  $Ni_2P$

nanosheets ( $\text{O}_3\text{-V}_{10}\text{-Ni}_2\text{P}$ ) treated by  $\text{O}_2$  plasma for 3 min gave the best performance. In the 1.0 M KOH solution,  $\eta_{10}\text{-HER}$  and  $\eta_{10}\text{-OER}$  were 108 mV and 257 mV, respectively. In addition, a smaller Tafel slope was obtained for HER (72.3 mV/dec) and OER (43.5 mV/dec). As comprehensive, dual-function catalysts for water electrolysis,  $\text{O}_3\text{-V}_{10}\text{-Ni}_2\text{P}||\text{O}_3\text{-V}_{10}\text{-Ni}_2\text{P}$  batteries required  $\eta_{10}$  to be only 1.563 V, which was superior to the most advanced  $\text{IrO}_2||\text{Pt/C}$  (1.687 V). The catalysts also had significant durability and 20 h of operational stability. These excellent properties were attributed to high-valence vanadium doping, which acted as a good electron acceptor and contributed to OER performance. Peng et al. [111] prepared nickel-doped amorphous FeP nanoparticle-supported titanium nitride nanowire array (Ni-FeP/TiN/CC) composites by high-energy metal ion implantation, which showed excellent HER performance in alkaline systems. The overpotential was 75 mV at a current density of  $10 \text{ mA/cm}^2$ , and the value remained at 93% of the initial value after continuous hydrogen evolution for 10 h at a high overpotential of 300 mV.

Cobalt phosphide is a new type of catalyst that has been developed in recent years to replace platinum metal-based electrocatalysts. However, the stability of cobalt phosphide is not as good as platinum, which limits the large-scale application of  $\text{CoP}_x$  in water electrolyzers. Goryachev et al. [112] prepared  $\text{Co}_3\text{O}_4$  films by plasma enhanced atomic layer deposition method, and obtained  $\text{CoP}_x$  electrodes by thermal phosphating ( $\text{PH}_3$ ), which has CoP and surface rich P ( $\text{P/CO} > 1$ ). It was found that the surface activation energy and the exchange current density was  $81 \pm 15 \text{ kJ/mol}$  and  $j_0 = -8.9 \times 10^5 \text{ A/cm}^2$ . Liu et al. [113] obtained plasma-activated (PA)-CoPO by the treatment of  $\text{Co}_3(\text{PO}_4)_2$  nanosheet arrays on a nickel network with  $\text{H}_2$  plasma, which had larger surface area, enhanced conductivity, rich coordination unsaturated  $\text{Co}^{3+}$ , and numerous oxygen vacancies. The catalysts showed excellent OER and HER performance. The voltages of oxygen evolution and hydrogen evolution were 240 mV and 50 mV at a current density of  $10 \text{ mA/cm}^2$ , and the Tafel slopes were 53 mV/dec and 35 mV/dec, respectively. Using a PA-CoPO nanosheet array as the anode and cathode, a full water split of  $10 \text{ mA/cm}^2$  was achieved at a low voltage of 1.48 V, which was superior to  $\text{IrO}_2/\text{C}-\text{Pt/C}$  at a sufficiently high overpotential. That provides a path for the design of high performance electrocatalysts for total hydrolysis, as shown in Figure 17e,f.

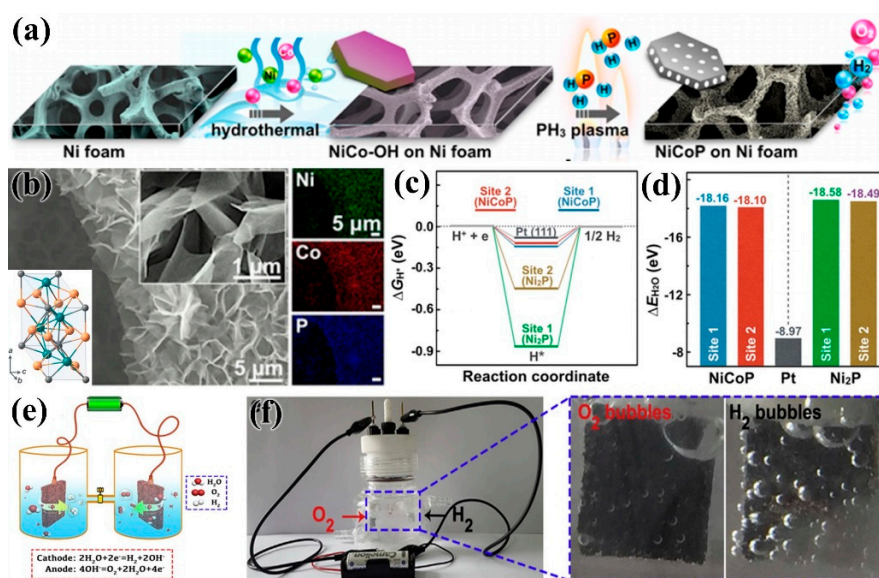


**Figure 17.** (a) Schematic diagram of the conversion of NiCo-OH nanosheets to NiCoP by  $\text{PH}_3$  plasma treatment; (b) SEM image, energy spectrum, and crystal structure of NiCoP; (c) free-energy diagram for  $\text{H}_2$  adsorption on the  $\text{Ni}_2\text{P}$ , NiCoP (0001), and Pt (111) surfaces; (d) adsorption energy of water [108] (Reproduced with permission from [108]. American Chemical Society, 2016.) (e) Schematic diagram of the bifunctional electrocatalysts OER and HER; (f) photograph of the water splitting in the alkaline solution at 1.5 V [113] (Reproduced with permission from [113]. Elsevier B.V., 2018).

### 3.7. Transition Metal Carbides

Nickel carbide ( $\text{Ni}_3\text{C}_x$ ) films are prepared by the  $\text{H}_2$  plasma atomic layer deposition technique. They are polycrystalline and highly homogeneous, with a rhombic  $\text{Ni}_3\text{C}$  crystal structure, and without any nanographite or amorphous carbon [114]. Xiong et al. [115] used the process to conformally coat a uniform thin layer of  $\text{Ni}_3\text{C}$  on carbon nanotubes (CNTs), in order to obtain core-shell nanostructured  $\text{Ni}_3\text{C}/\text{CNT}$  composites. The ALD-prepared  $\text{Ni}_3\text{C}/\text{CNT}$  composite exhibited excellent performance in supercapacitors and electrocatalytic hydrogen evolution. Ko et al. [116] used plasma-assisted deposition to grow WC nanowalls from bottom to top on a silicon wafer, which were highly crystalline and showed superior HER performance in a 0.5 M  $\text{H}_2\text{SO}_4$  solution. Not only was the Tafel slope 67 mV/dec, but also oxidation would not occur even after 10,000 cycles of recycling, which displayed good durability.

### 3.8. Other Compounds

In 2018, Guo et al. [117] performed a non-destructive modification of the Prussian blue analog (PBA) structure by air plasma. The reactive oxygen species produced by plasma selectively bound to the metal in the framework, while retaining the porous structure of the framework with the high dispersion and orderliness of metal sites in the framework. Porous catalyst Co-PBA-plasma 2 h was obtained with extremely high oxygen evolution activity. Prussian blue was a Fe/Co double metal cyanide skeleton composed of cyanide bridged Fe and Co cations (Figure 18a–c). The reactive oxygen species generated in the plasma were bonded to the open sites of Co, promoting the oxidation state transition of Co to Co(III) (Figure 18d). Due to the highly reactive metal catalytic sites in the nanoporous framework, the OER catalysts showed a low overpotential characteristic of only 330 mV at a high current density of 100  $\text{mA}/\text{cm}^2$ . This value is close to the actual operating conditions of industrial alkaline materials, implying a very promising technology for developing high performance catalysts. Yan et al. [118] used Ar plasma to prepare phytic acid- $\text{Co}^{2+}$  (P-Phy- $\text{Co}^{2+}$ ) with coordination unsaturation, which had an oxygen evolution potential of 306 mV at a current density of 10  $\text{mA}/\text{cm}^2$ . The method can be extended to CoFe bimetallic system. The oxygen evolution potential of P-Phy- $\text{Co}^{2+}/\text{Fe}^{3+}$  prepared at the current density of 10  $\text{mA}/\text{cm}^2$  was 265 mV, and the Tafel slope was less than 36.51 mV/dec.

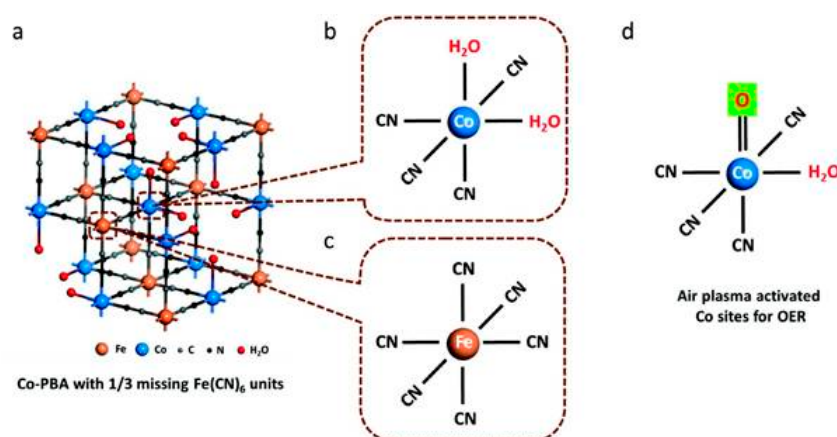


**Figure 18.** (a) The structure of Co-PBA with the composition of  $\text{Co}_3(\text{Fe}(\text{CN})_6)_2$ ; the coordination structure of (b) Co and (c) Fe sites. Each Co center has two open sites, which are occupied by coordinated water molecules, while the Fe center is completely coordinated by six CN groups; (d) schematic diagram of metal sites in Prussian blue's structure modified by air plasma [117]. (Reproduced with permission from [117]. Wiley-VCH, 2018).

#### 4. Carbon Based Electrocatalysts

Carbon is one of the most abundant and important elements in nature. Carbon-based catalysts have become one of the most popular electrocatalysts in recent years [119]. Carbon-based materials have more advantages than traditional materials, such as low costs, various structures, and good electrical and thermal conductivity. The excellent catalytic performance can be obtained by tailoring carbon-based materials with specific sizes, doping types, contents, morphologies and structures, promoting active site exposure, increasing the transport of reaction-related substances, and enhancing the transfer of electrons throughout the electrode [120,121]. At the same time, more defects become the active sites of the electrocatalyst after heteroatom doping. In addition, intrinsically defective carbon electrode catalysts also exhibit catalytic activity comparable to carbon materials doped with heteroatoms (e.g., F, S, P, and B) [122].

##### 4.1. Defective Carbon Materials

Defective carbon materials have also attracted attention for enhancing electrocatalytic activity. Generally, defect-rich materials are prepared at elevated temperatures or using template precursors to form more edge and hole defects [123]. In 2016, Tao et al. [124] obtained defect-rich graphene and carbon nanotubes by using Ar plasma to etch the surface of graphene and carbon nanotubes, as shown in Figure 19a–e. The P-CNTs acquired with plasma treatment had also many defects.

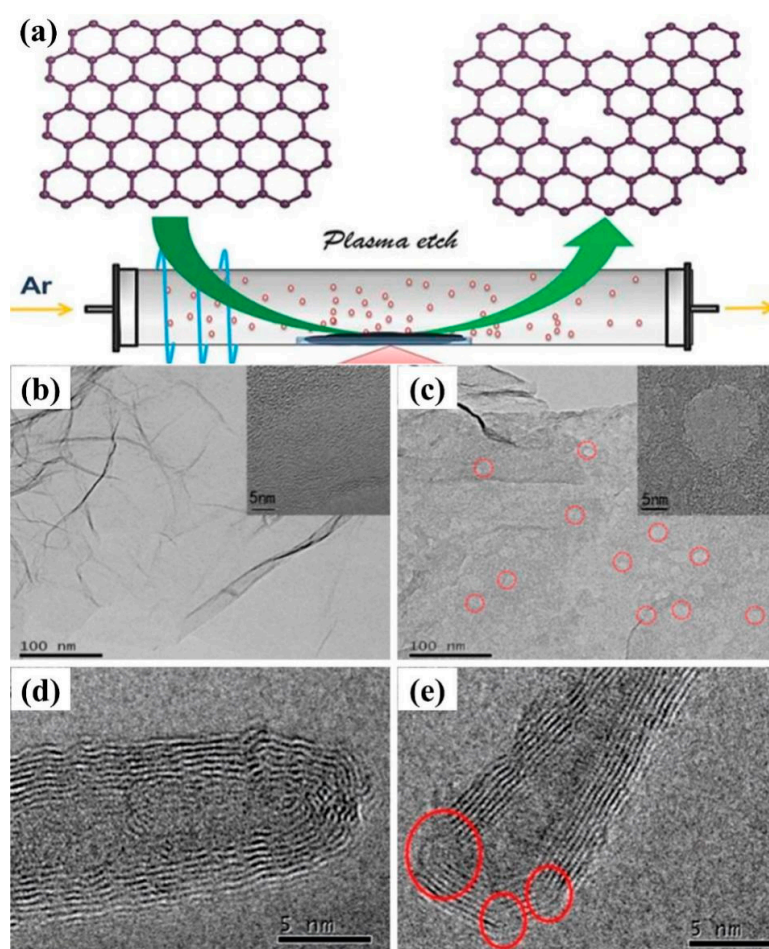


**Figure 19.** (a) Schematic diagram of the preparation of Ar plasma etching graphene and carbon nanotubes surface by Ar plasma; TEM images of (b) graphene and (c) Ar plasma treated graphene; TEM images of (d) carbon nanotubes and (e) Ar plasma treated carbon nanotubes [124]. (Reproduced with permission from [124]. Royal Society of Chemistry, 2016).



Subsequently, Liu et al. [125] directly treated commercial carbon cloth with Ar plasma technology and exposed it to air, which not only made the surface of carbon fiber more rough and porous, but also exposed more graphene-like nanosheets on the surface. And the deficient, oxygen-doped graphene was also produced in situ on its surface. Compared with pure carbon cloth, the distance between carbon nanosheets was about 0.37 nm after simple plasma etching of carbon cloth P-CC, which was larger than that of graphite  $d_{002} = 0.34$  nm. The value of  $SP^2/SP^3$  of carbon was significantly reduced, which means that plasma treatment can produce more defects. The carbon fibers after plasma etching exhibited a larger specific surface area, exposing more active sites, and the treated carbon fibers had better conductivity, making them more conducive to material transfer, resulting in better catalytic performance in OER and ORR. An amorphous, edge-rich/defective graphene was generated in situ on the surface of the carbon fibers by argon plasma etching, while the dangling bonds of these defect sites were exposed to air and reacted with oxygen or water to achieve oxygen functionalization. In 2018, Lehmann et al. [126] used plasma-enhanced chemical vapor deposition to prepare defect-rich layered carbon nanowalls (hCNW) with readily accessible graphite edge locations at the top of the wall and many defect locations within the porous sidewalls, which was considered to be the ideal sites for adsorption and electron transfer. And the ORR initiation potential of hCNW-60 in 0.1 M KOH solution was 830 mV with a two electron transfer.

#### 4.2. Nitrogen-Doped Carbon Materials

The doping of nitrogen atoms in graphene is considered to be a good way to improve the electrocatalytic performance. Wang et al. [127] mainly prepared N-doped graphene oxide (N-PEGO) by low temperature plasma technology. Ammonium carbonate was used as the activator and nitrogen source in the preparation of N-PEGO by low temperature plasma technology, which can effectively achieve the exfoliation of graphene oxide and nitrogen doping in one step (Figure 20). The N-PEGO prepared by this method has a nitrogen doping amount of 5.3 at%, a specific surface area of 380.0  $m^2/g$ , an initial potential of 0.89 V (versus RHE), and an excellent oxygen reduction reaction (ORR) catalysis, which also showed better stability and methanol resistance than the commercial noble metal Pt/C catalysts. Zhu et al. [128] achieved nitrogen doping of graphene foam by  $N_2$  plasma technology (NGF-CFP), which exhibited excellent OER performance.

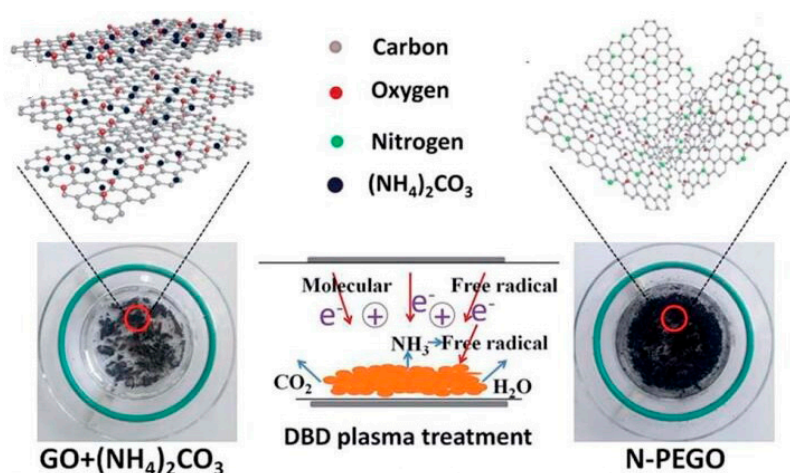


**Figure 20.** Schematic diagram of N-doped graphene oxide prepared by low temperature plasma technology [127]. (Reproduced with permission from [127]. Royal Society of Chemistry, 2018).

N-doped carbon nanotubes are also used as electrocatalysts [129]. In 2015, Du et al. [130] successfully synthesized nitrogen-doped carbon nanotubes (NCNTs) with a nitrogen content of 5.38 at.% via microwave plasma chemical vapor deposition (MPCVD). Because of the doping of nitrogen, NCNT exhibited the same ORR electrocatalytic activity as Pt-CNT, which was 0.87 V of

the initial point and 4.1 of the electron transfer number, and had the highest ORR performance at a load of 729  $\mu\text{g}/\text{cm}^2$ . Subramanian et al. [131] prepared carbon nanotube carpets (VA-NCNTs) with nitrogen-doped vertical alignment by treating carbon nanotubes with  $\text{N}_2$  plasma. Compared with undoped nitrogen VA-CNTs, VA-NCNTs exhibited well electrocatalytic performance under alkaline conditions. Zhang et al. [132] obtained NCNT/glass carbon (GC) electrode by treating carbon nanotubes with  $\text{NH}_3$  plasma, which can reduce  $\text{CO}_2$  to formate in water without using metal catalysts. If polyethyleneimine (PEI) is coated on NCNT/GC electrode, the catalytic overpotential can be significantly reduced, and the current density and efficiency can be increased, which is helpful for stabilizing the intermediate of the  $\text{CO}_2$  reduction of PEI.

The plasma deposition method and the solution plasma method are considered to be effective methods for one-step synthesis of nitrogen-doped carbon nanoparticles (NCNP) [133,134]. NCNPs can be synthesized in situ by solution plasma, and the type of C–N bond can be controlled by the structure of precursors and additives (Figure 21a–c). Li et al. [135] prepared different NCNPs using pyridine and acrylonitrile as heterocyclic and linear structure precursors, and using ruthenium as additives, which can realize the control of nitrogen elements (Figure 21d–g). It was found that the current density was proportional to the content of graphite-N. The existence of graphite-N promoted the direct four-electron transfer pathway of ORR, while the higher percentage of amino-N made the ORR initiation potential move to a positive value. Amino-N and graphite-N played a synergistic role in improving ORR activity. Li et al. [136] produced N-doped carbon nanoparticles by solution plasma containing pyridine-N, amino-N, and graphite-N bonds, which provided a simple and effective method to study the relationship between C–N bonding structure and the electrochemical performance of N-doped carbon catalysts. At the same time, Panomsuwan et al. [137,138] obtained NCNPs samples with different nitrogen doping content (0.63–1.94 at.%) by changing the difference of C/N molar ratio in organic precursors, using organic liquid mixtures such as benzene and pyrazine as precursors. It was found that the initial potential and current density of the ORR electrochemical properties of NCNP were improved with the increase of nitrogen doping content, which was mainly due to the graphite-N and pyridine-N on NCNPs. Compared to commercial Pt/C catalysts, NCNP showed superior long-term durability and strong methanol tolerance.

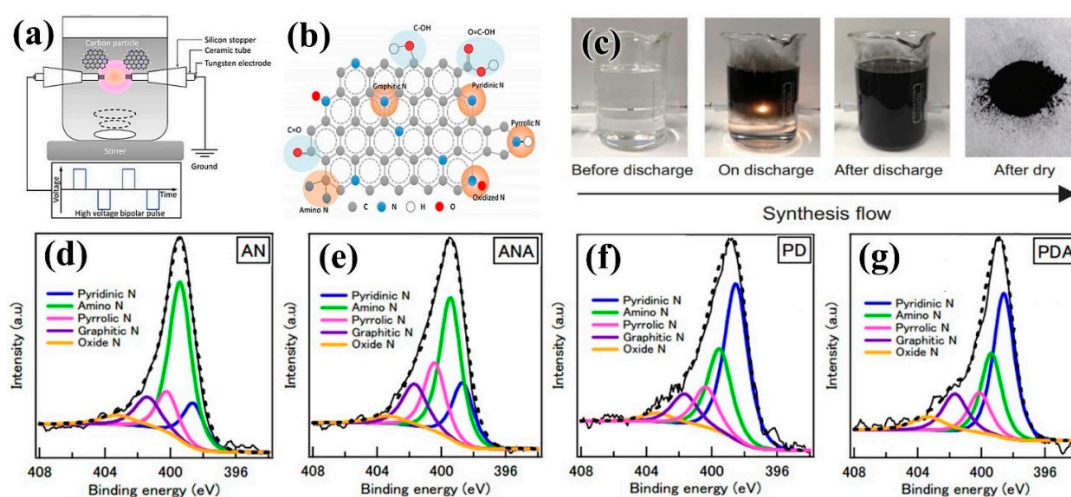


**Figure 21.** (a) Schematic diagram of preparation of N-doped carbon nanoparticles (NCNP) by solution plasma method; (b) species of doped single atoms [135] (copyright © 2017 Royal Society of Chemistry.) (c) Process for preparing nano-carbon materials by solution plasma method [139] (open access.) (d–g) Distribution of nitrogen elements of NCNP prepared from acrylonitrile (AN), acrylonitrile + ANA, pyridine (PD), and pyridine + hydrazine (PDA) as precursors [135]. (Reproduced with permission from [135]. Royal Society of Chemistry, 2017).

#### 4.3. Oxygen-Doped Carbon Materials

The solution plasma method can also be used to synthesize carbon nanoparticles containing oxygen in one step. Ishizaki et al. [140] successfully synthesized oxygen-containing carbon nanomaterials using a mixture of benzene (BZ) and 1,4-dioxane (DO). Although DO content did not affect the initial potential, it did influence the current density of ORR. With the increase of DO content, the O contents in the samples increased, such that the order of current density of ORR carbon nanosamples was as follows: BZ90 + DO10 > BZ100 > BZ70 + DO30 > BZ50 + DO50. Kondratowicz et al. [141] used oxygen plasma to adjust the properties of reduced graphene oxide (rGO), which was an easy-to-control and eco-friendly method. Oxygen plasma treatment can improve the adsorption of enzymes on rGO electrodes by introducing oxygen groups and increasing porosity. With different plasma treatment times, different oxygen groups (such as carboxyl and hydroxyl groups) can be introduced on the surface of rGO to change the wettability of rGO, and other functional groups (such as quinones and lactones) can also be produced in a longer treatment time. In addition, the external surface of rGO was partially etched, resulting in an increase in surface area and porosity of the material. The current density of rGO treated for 10 min was twice as high as that of untreated rGO.

#### 4.4. Sulfur-Doped Carbon Materials

Sulphur atom doping can effectively change the electronic and chemical properties of graphene, making it possible for graphene to be used as the electrocatalyst. In 2016, Wang et al. [142] realized the reduction of graphene oxide and doping of S with the treatment of microwave-assisted stripping and hydrogen sulfide plasma. Sulfur-doped graphene was used for an ORR electrocatalytic reaction under alkaline conditions, showing excellent electrochemical performance. In 2017, Ting et al. [143] etched sulfur-doped graphene by Ar plasma, resulting in more topological defects, while maintaining the original doping structure of SG (Figure 22a). Benefiting from the synergistic coupling of S-doping and plasma-induced topographic defects, SG-P had greatly enhanced HER activity and good stability in acidic media, demonstrated by its low overpotential of 178 mV at the current density of 10 mA/cm<sup>2</sup>, and Tafel slope of 86 mV/dec. The optimum HER activity of SG-P can be obtained by combining thiophene-rich substances with appropriate plasma-induced topological effects (Figure 22b–g). In 2018, Zhou et al. [144] obtained the self-supporting electrode 3DSG-Ar by Ar plasma treatment of three-dimensional sulfur-doped graphene (3DSG), which showed excellent HER electrocatalytic activity. After 2000 cycles, it still had good electrocatalytic stability, and the Tafel slope was 64 mV/dec.

#### 4.5. Boron-Doped Carbon Materials

Panomsuwan et al. [145] prepared boron-doped carbon nanoparticles (BCNP) by solution plasma process using benzene and triphenyl borate as precursors (Figure 23). Compared with undoped carbon nanoparticles, the electrocatalytic activity of BCNP for oxygen reduction reaction (ORR) in alkaline solution was improved in terms of initial potential and current density. In addition, BCNP showed excellent long-term durability and methanol oxidation resistance in ORR. Li et al. [146] obtained porous BDD/Ta multilayers by etching polycrystalline boron-doped diamond (BDD) on tantalum substrates with H<sub>2</sub>/Ar plasma. It was found that the effective electroactive surface area and charge transfer ability of etched microcrystals at liquid crystal interface were improved. The porous BDD/TA electrodes were applied to electro-Fenton method for rapid degradation of methylene blue.

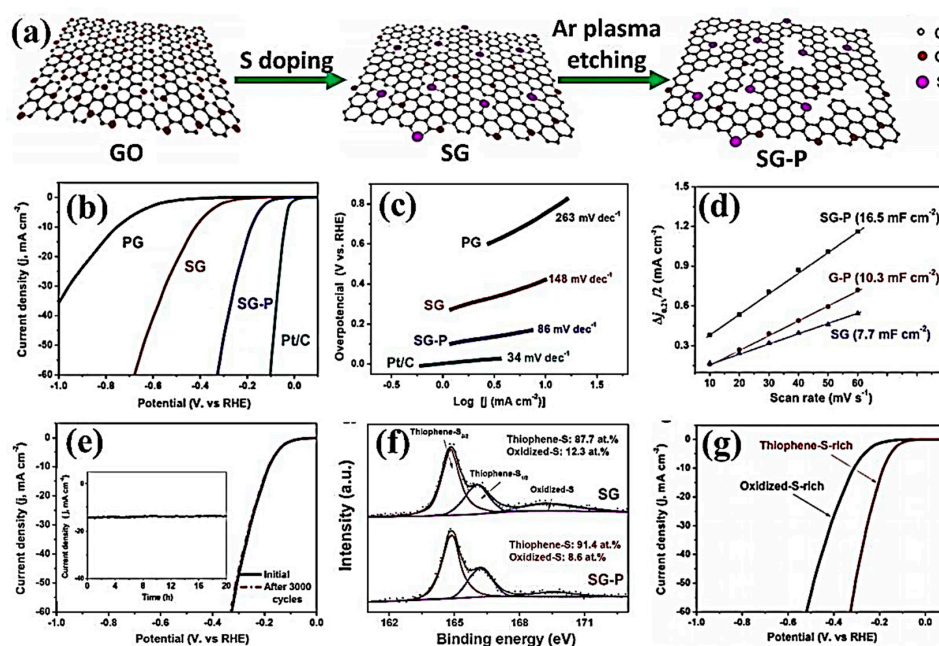


**Figure 22.** (a) Schematic diagram of the treatment of S-doped graphene BY Ar plasma. (b) Polarization potential and (c) Tafel slope at a scan speed of 5 mV/s in a 0.5 M H<sub>2</sub>SO<sub>4</sub> solution of PG, SG, SG-P, and commercial 20% Pt/C. (d) Current densities of SG, G-P, and SG-P. (e) Cycle performance of SG-P. (f) PG, SG, SG-P, and commercial 20% Pt/C of S's 2p for SG and SG-P. (g) Different polarization curves for SG-P enriched in thiophene sulfur and oxidized sulfur [143]. (Reproduced with permission from [143]. Elsevier B.V., 2017).

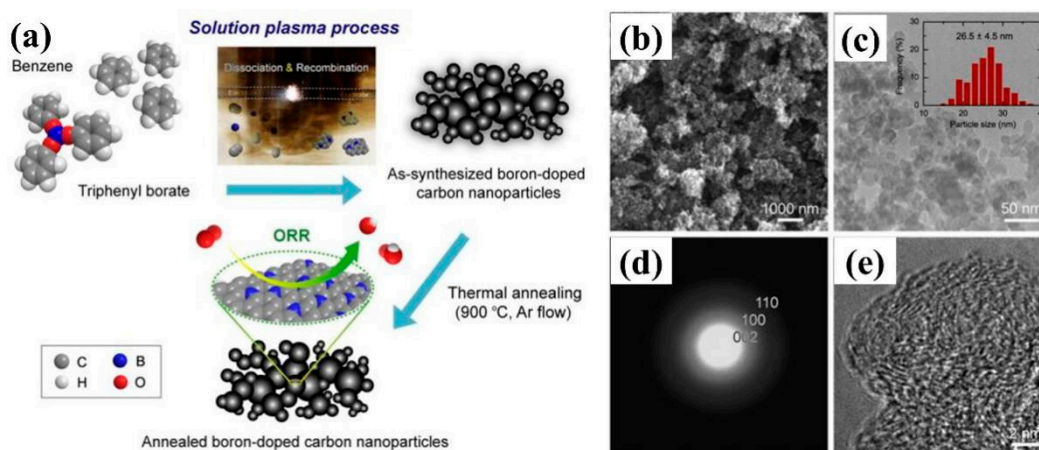


**Figure 23.** (a) Schematic diagram of the preparation of B-doped nanoparticles (BCNP) by solution plasma. (b) SEM image, (c) TEM images, and particle size distribution image; (d) SAED diffraction pattern; and (e) HRTEM images of BCNP [145]. (Reproduced with permission from [145]. Elsevier B.V., 2015).

Table 1. Preparation of electrocatalysts by plasma technology.

Reaction Type	Samples	Methods	Electrochemical Performance	Ref.
MOR	Pt/TiO <sub>2</sub>	PEALD	the MOR current density drops to a small value after 1500 s with NCALD < 30.	[15]
	Pt/C	CAPD	The calculated ECSAs of 75.4 m <sup>2</sup> /g	[16]
	Pt/GNT	H <sub>2</sub> plasma	The current density of 97.9 mA/mg and mass activity of 691.1 mA/mg Pt	[20]
	Pt/CNTs-HP	H <sub>2</sub> plasma	The current density of 15.8 mA/mg	[21]
	Au@Pt	Ar plasma	Mass activity up to 48 ± 3 m <sup>2</sup> /g	[23]
	Pt-Ag	SPS	The calculated ECSAs of 28.15 m <sup>2</sup> /g	[27]
	Pt <sub>40</sub> Pd <sub>60</sub>	SPS	The calculated ECSAs of 28.15 m <sup>2</sup> /g	[28]
	Pt <sub>69</sub> Pd <sub>31</sub>	SPS	The catalytic activity of 6.81 mA/cm <sup>2</sup>	[29]
	PtPd/KB-2	SPS	The electrocatalytic activity was more than 4 times of that of commercial Pt/C	[30]
	Pt/CoPt/MWCNS	SPS	Mass activities of 1719 mA/mg Pt	[32]
	Pt/C/TiO <sub>2</sub> -2	SPS	Mass activities of 315.2 mA/mg Pt	[33]
	Pt-Ru/OCNT	O <sub>2</sub> plasma	The onset potential of 0.3 V	[44]
	Pt/ZnO/KB	SPS	Catalytic activity of 964 mA/mgPt	[48]
OER	Pt-Ir/TiC	Ar plasma	The current density of 2.5 mA/cm <sup>2</sup> at 1 V	[22]
	PtO <sub>a</sub> PdO <sub>b</sub> @Ti <sub>3</sub> C <sub>2</sub> T <sub>x</sub>	SPS	Activation potential of 1.5 V in 0.1 M KOH	[40]
	Ag/1400-15	Spark plasma sintering	The value of 61 mV	[41]
	CoNPs@C	MPECVD	Overpotential of 270 mV	[50]
	CoO-N/C	Cold plasma deposition	The oxygen evolution potential of 378 mV	[55]
	Co <sub>3</sub> O <sub>4</sub> nanosheets	Ar plasma	The current density of 44.44 mA/cm <sup>2</sup> at 1.6 V	[60]
	V <sub>o</sub> -COOH	Ar plasma	The low overpotential of 262 mV at 10 mA/cm <sup>2</sup>	[61]
	Co <sub>3</sub> O <sub>4-x</sub>	Ar plasma	The overpotential of 330 mV and Tafel slope of 58 mV/dec	[62]
	N-Co <sub>3</sub> O <sub>4</sub>	N <sub>2</sub> plasma	The required potential of 1.54 V to reach the current density of 10 mA cm <sup>-2</sup>	[64]
	P-Co <sub>3</sub> O <sub>4</sub>	Ar plasma	The overpotential of 280 mV and Tafel slope of 51.6 mV/dec	[67]
	CoO <sub>x</sub> -ZIF	O <sub>2</sub> plasma	The required potential of 1.548 V to reach the current density of 10 mA cm <sup>-2</sup>	[69]
	SnCoFe-Ar	Ar plasma	The overpotential of 300 mV and Tafel slope of 42.3 mV/dec	[71]
	SrTi <sub>0.5</sub> Fe <sub>0.5</sub> O <sub>3-y</sub>	HT-PVD using O <sub>2</sub> plasma	The onset potential of 1.40 at 100 μA	[72]
	SCFP-NF	High-energy argon plasma sputtering	The ultra high mass activity of 1000 mA/mg	[73]
	CoFe-LDHs-H <sub>2</sub> O	H <sub>2</sub> O plasma	The overpotential of only 232 mV	[74]
	CoFe-LDHs-Ar	Ar plasma	The overpotential of only 232 mV at a current density of 10 mA/cm <sup>2</sup>	[77]
	CoFe-LDHs-N <sub>2</sub>	N <sub>2</sub> plasma	The overpotential of only 233 mV at a current density of 10 mA/cm <sup>2</sup>	[78]
	FeO <sub>x</sub> /C	pulsed arc plasma deposition	The discharge specific capacity of 500 mAh/g under 100 mA/g	[80]
Co <sub>9</sub> S <sub>8</sub> /G	NH <sub>3</sub> plasma	The Tafel slope of 82.7 mV/dec	[91]	
Cu <sub>2</sub> S/CF	active iodine DBD plasma	The overpotential of 290 mV at a current density of 10 mA/cm <sup>2</sup>	[93]	
CoS/Ni <sub>3</sub> S <sub>2</sub> -FeS/PNFF	Air plasma	The overpotential of 136 mV at a current density of 10 mA/cm <sup>2</sup>	[96]	

Table 1. Cont.

Reaction Type	Samples	Methods	Electrochemical Performance	Ref.
	hNi <sub>3</sub> N	N <sub>2</sub> plasma	The overpotential of 325 mV at a current density of 10 mA/cm <sup>2</sup>	[101]
	NiCoP	PH <sub>3</sub> Plasma	The overpotential of 280 mV at a current density of 10 mA/cm <sup>2</sup>	[108]
	NiFePi/P	PECVD	The overpotential of 230 mV at a current density of 10 mA/cm <sup>2</sup>	[109]
	O <sub>3</sub> -V <sub>10</sub> -Ni <sub>2</sub> P	O <sub>2</sub> plasam	The Tafel slope of 43.5 mV/dec	[110]
	PA-CoPO	H <sub>2</sub> plasma	The overpotential of 240 mV and Tafel slope of 53 mV/dec	[113]
	Co-PBA-plasma 2 h	Air plasma	The overpotential of 330 mV at a current density of 100 mA/cm <sup>2</sup>	[117]
	NGF-CFP	N <sub>2</sub> plasma	The current density of 10 mA/cm <sup>2</sup> at 2.16 V	[128]
SO <sub>2</sub> OR	Pt <sub>3</sub> Pd <sub>2</sub> and PtPd <sub>4</sub>	Plasma sputtering	The lower onset potential of 0.587 ± 0.004 V	[18]
HOR	Pt/C	SPS	The ECSAs value of 266 cm <sup>2</sup> /mg	[38]
AMXOR	Ti <sub>4</sub> O <sub>7</sub>	Plasma deposition	A quick oxidation of 0.1 mM AMX	[79]
	Pt/C	CAPD	The half-wave potential of 0.87 V	[16]
	Pt-Ir/TiC	Ar plasma	Nyquist plots of 0.6 V	[22]
	Au@Pt	Ar plasma	The peak potential of 0.75 V	[23]
	Pt/XC72	SPS	The onset potential of 1.04 V	[31]
	PdAu/KB	SPS	The reduction peak disappeared after about 700 cycles	[34]
	AgNW/C	SPS	The high electron density of 13.7 × 10 <sup>-22</sup> m <sup>-3</sup>	[37]
	Pt/rGO-N	SPS	The half-wave potential of 0.87 V	[39]
	Ag/1400-15	spark plasma sintering	The electron transfer number of 3.9	[41]
	PtNW/GDL	N <sub>2</sub> + H <sub>2</sub> plasma	The power density of 64 mW/cm <sup>2</sup>	[47]
	CoO-N/C	Cold plasma deposition	A 2-electron process producing H <sub>2</sub> O <sub>2</sub>	[55]
	Ag@Co <sub>3</sub> O <sub>4</sub>	SPS	The half-wave potential of 0.799 V	[56]
	15Co <sub>3</sub> O <sub>4</sub> /N-AP/800	microwave-induced plasma	The Tafel slope of 42 mV/dec	[57]
	Co-La-Pt	DC arc discharge plasma	The specific capacity of 3250.2 mAh/g and energy density of 8574.2 Wh/kg at 0.025 mA/cm <sup>2</sup>	[58]
	Co <sub>3</sub> O <sub>4-x</sub>	Ar plasma	The half-wave potential of 0.84 V	[62]
	FeO <sub>x</sub> /C	Pulsed arc plasma deposition	The discharge specific capacity of 500 mAh/g under 100 mA/g	[80]
ORR	MnO <sub>x</sub> @C-D	Air plasma	The electron transfer number of 3.81	[81]
	A-MnO <sub>2</sub>	Ar plasma	The power density of 159 mW/cm <sup>2</sup> at a current density of 157 mA/cm <sup>2</sup>	[82]
	Cu <sub>3</sub> N <sub>200</sub> /C	PEALD	The half-wave potential of 0.684 V	[103]
	Fe-N-CNP-CN	SPS	The onset potential of -0.10 V	[104]
	Fe-N/C	Air plasma	The onset potential of 0.88 V at a loading of 0.60 mg/cm <sup>2</sup>	[105]
	P-Graphene	Ar plasma	The onset potential of 0.912 V and half-wave potential of 0.737 V	[124]
	P-CNTs	Ar plasma	The onset potential of 0.83 V	[124]
	P-CC	Ar Plasma	The exchange current density of 2.57 × 10 <sup>-9</sup> A/cm <sup>2</sup>	[125]
	hCNW-60	PECVD	The onset potential of 830 mV in 0.1 KOH	[126]

Table 1. Cont.

Reaction Type	Samples	Methods	Electrochemical Performance	Ref.
	N-PEGO	DBD plasma	The onset potential of 0.89 V	[127]
	NCNTs	MPCVD	The onset potential of 0.87 V and the electron transfer number of 4.1	[130]
	VA-NCNTs	N <sub>2</sub> plasma	The ORR peak at the potentials of about −0.3 V	[131]
	NCNPs	SPS	The onset potential of −0.17 V	[137]
	NCNP-3	SPS	The onset potential of −0.143 V	[138]
	BZ90 + DO10	SPS	The samples were held at 0.5 V with a rotation speed of 1500 rpm for 45,000 s in an O <sub>2</sub> -saturated 0.1 M KOH solution	[140]
	O-rGO	O <sub>2</sub> Plasma	The current density of 10 μA/cm <sup>2</sup>	[141]
	BCNP	SPS	The current densities of 3.15 mA/cm <sup>2</sup> at −0.60 V	[145]
	FCNP-4	SPS	The onset potential of 0.22 V and limiting current density of 2.76 mA/cm <sup>2</sup> at 0.6 V	[147]
	BCN nanocarbon	SPS	15.1% current decrease after 20000 s	[149]
CO <sub>2</sub> RR	Au island	O <sub>2</sub> plasma	The faradaic efficiency over 95%	[24]
	CNT/Cu	O <sub>2</sub> plasma	Carbon monoxide yields of 178 mmol cm <sup>2</sup> mA <sup>−1</sup> h <sup>−1</sup>	[51]
	Cu foil	O <sub>2</sub> plasma	The ethylene selectivity of 60%	[52]
	Cu nanocube	O <sub>2</sub> plasma	The ethylene selectivity of 60%	[53]
	ZnO	H <sub>2</sub> plasma	The current density of −16.1 mA/cm <sup>2</sup> and faradaic efficiency of 83%	[84]
	PEI-NCNT/GC	NH <sub>3</sub> plasma	The current density of 2.2 mA/cm <sup>2</sup>	[132]
HER	Ni-Fe-C	CH <sub>4</sub> +H <sub>2</sub> Plasma carburizing	The activation potential of 57 mV at a current density of 10 mA/cm <sup>2</sup>	[49]
	CoNPs@C	MPECVD	The overpotential of 153 mV at a current density of 10 mA/cm <sup>2</sup>	[50]
	P-Co <sub>3</sub> O <sub>4</sub>	Ar plasma	The overpotential of 120 mV and Tafel slope of 52 mV/dec	[67]
	SCFP-NF	high-energy argon plasma sputtering	The onset potential of −0.01 V and Tafel slope of 94 mV/dec	[73]
	C-30s	C plasma	The Tafel slope of 44 mV/dec	[83]
	TaS <sub>2</sub> -15 min	O <sub>2</sub> plasma	The onset potential of 310 mV	[85]
	O <sub>2</sub> -MoS <sub>2</sub>	O <sub>2</sub> plasma	The current density of 16.3 mA/cm <sup>2</sup> at −350 mV	[86]
	MoS <sub>2</sub>	O <sub>2</sub> plasma	The overpotential of 131 mV at a current density of 10 mA/cm <sup>2</sup>	[87]
	H <sub>3</sub> Mo <sub>12</sub> O <sub>40</sub> P/MoS <sub>2</sub>	O <sub>2</sub> plasma	The Tafel slope of 44 mV/dec	[88]
	MoS <sub>2</sub> -15 min	H <sub>2</sub> plasma	The overpotential of 240 mV at a current density of 10 mA/cm <sup>2</sup>	[89]
	MoS <sub>1.7</sub>	H <sub>2</sub> plasma	The overpotential of 143 mV at a current density of 10 mA/cm <sup>2</sup>	[90]
	Co <sub>3</sub> S <sub>4</sub> PNSvac	Ar plasma	The mass activity of 1056.6 A/g at an overpotential of 200 mV	[92]
	WS <sub>2</sub>	PEALD	The overpotential of 90 mV at a current density of 100 mA/cm <sup>2</sup>	[94]
	WS <sub>2</sub>	SF <sub>6</sub> /C <sub>4</sub> F <sub>8</sub> plasma-etched	The overpotential of 100 mV and Tafel slope of 50 mV/dec	[95]
	CoS/Ni <sub>3</sub> S <sub>2</sub> -FeS/PNFF	Air plasma	The overpotential of 75 mV at a current density of 10 mA/cm <sup>2</sup>	[96]
N-MoSe <sub>2</sub> /VG	MPECVD	The onset potential of 45 mV and overpotential of 98 mV at 10 mA/cm <sup>2</sup>	[98]	
MoSe <sub>2</sub> /Mo	N <sub>2</sub> /H <sub>2</sub> plasma	The Tafel slope of 34.7 mV/dec	[99]	
Ni <sub>3</sub> N <sub>1-x</sub> /NF	Microwave plasma	The overpotential of 55 mV and Tafel slope of 54 mV/dec at a current density of 10 mA/cm <sup>2</sup>	[102]	

Table 1. Cont.

Reaction Type	Samples	Methods	Electrochemical Performance	Ref.
	NiCoP	PH <sub>3</sub> plasma	The overpotential of 32 mV at a current density of $-10 \text{ mA/cm}^2$	[108]
	O <sub>3</sub> -V <sub>10</sub> -Ni <sub>2</sub> P	O <sub>2</sub> plasma	The overpotential of 108 mV and Tafel slope of 72.3 mV/dec	[110]
	Ni-FeP/TiN/CC	Plasma-implanted method	The overpotential of 75 mV at a current density of $10 \text{ mA/cm}^2$	[111]
	CoP <sub>x</sub>	PEALD	The exchange current density of $-8.9 \times 10^5 \text{ A/cm}^2$	[112]
	PA-CoPO	H <sub>2</sub> plasma	The overpotential of 50 mV at a current density of $10 \text{ mA/cm}^2$	[113]
	WC nanowalls	DC-PACVD	The Tafel slope of 67 mV/dec	[116]
	Co-PBA-plasma 2 h	Air plasma	The overpotential of 77 mV at a current density of $20 \text{ mA/cm}^2$	[117]
	SG-P	Ar plasma	The overpotential of 178 mV at a current density of $10 \text{ mA/cm}^2$	[143]
	3DSG-Ar	Ar plasma	The Tafel slope of 64 mV/dec	[144]
	P-NSG	Ar plasma	The onset potential of 58 mV	[148]



#### 4.6. Fluorine-Doped Carbon Materials

Fluorine-doped carbon nanoparticles (FCNPs) can also be prepared by the solution plasma method. Panomsuwan et al. [147] used the mixture of toluene and trifluorotoluene as the precursor to prepare FCNPs, whose fluorine doping content can range from 0.95 to 4.52 at%. The obtained FCNPs mainly exhibited disordered amorphous structure, and the incorporation of fluorine atoms resulted in more defect sites and disordered structures in carbon particles. With the increase of fluorine doping content, the ORR electrocatalytic activity of FCNPs had been significantly improved, which was mainly due to the intercalation of ionic C–F and semi-ionic C–F bonds in the carbon structure. Compared with commercial Pt-based catalysts, FCNP exhibited excellent long-term operational durability and strong tolerance to methanol oxidation.

#### 4.7. Heteroatom Co-Doped Carbon Materials

Diatomic co-doping is also considered as one of the effective strategies to improve the catalytic activity of carbon-based electrocatalysts. Tian et al. [148] obtained defect-rich P–NSG samples by the etching of N and S co-doped graphene (NSG) with Ar plasma. The synergistic coupling of N and S co-doping and plasma-induced structural defects maximized the number of active sites of graphene, which significantly improved the HER catalytic activity of P–NSG in both acidic and alkaline media. Lee et al. [149] synthesized boron–carbon–nitrogen (BCN) nanocarbon materials by solution plasma method in one step. The synergistic effects of N and B at the state of uncoupled bonding changed the electronic structure of basic carbon and promoted the formation of new ORR active sites. Although the electron transfer number of BCN nanocarbon was 3.43, and the ORR activity was not as good as commercial Pt/C, the current only decreased by 15.1% after 20,000 s, which was obviously better than commercial Pt/C (under the same conditions, the current decreased by 61.5%).

### 5. Conclusions and Prospects

Electrocatalytic materials have been widely used in energy and environmental fields, such as electrocatalytic hydrogen production, the reduction of carbon dioxide, fuel cells, the N<sub>2</sub> reduction of ammonia, and so on. Noble metals have high energy utilization efficiency and excellent catalytic performance, but they have the disadvantages of poor availability and high prices. Therefore, it is important to develop highly active metal catalysts with low mass loading and high dispersibility. In recent years, researchers have focused on non-noble metal-based catalysts with low costs, high catalytic activities and long lives, such as transition metal catalysts, oxides, sulfides, nitrides, phosphides, and carbides. At the same time, carbon-based catalysts have been favored by researchers because of their superior electrocatalytic performances in both acidic and alkaline systems. The plasma device has a simple and adjustable structure, which can be used to prepare and modify the electrocatalysts.

In the preparation of electrocatalysts by plasma, different types of plasma may have different effects on the materials. The plasma can assist the precursor of gas or liquid-derived atoms, molecules, ions, or radicals to drive the synthesis of electrocatalysts. For example, the plasma deposition method can directly prepare a catalyst material with low loading and excellent dispersibility; the solution plasma can directly synthesize noble metal catalysts, noble metal alloy catalysts, and hetero atom-doped carbon-based catalysts; as a “bottom-up” synthesis technology, low-temperature plasma can be directly used to prepare specific nanostructured electrocatalysts. However, how to further improve the efficiency of plasma-assisted synthesis and expand its application in large-scale industrial production, is still challenging.

Plasma can achieve “top-down” denudation or surface treatment in plasma modification of electrocatalysts. Since the electrocatalytic process often occurs on the surface of catalysts, the structure regulation of the surfaces of catalysts by plasma can effectively improve the catalytic activities of electrocatalysts. Firstly, electrocatalysts with uniform dispersion and small particle sizes of active components can be obtained by plasma modification of the carrier or active component of

electrocatalysts; secondly, plasma etching can be used to expose more interfacial defects on the surface of electrocatalysts and increase the catalytic active sites on the edge; thirdly, some heteroatoms (such as N, S, B, and P) can be doped by plasma to enhance the intrinsic defects, realizing the catalytic activity of electrocatalysts. Defects have been recognized as active sites with higher activity in electrocatalytic reactions (vacancies, marginal sites, and lattice defects). At present, how to precisely control and tailor the defects of the electrocatalysts, the surface modifications, and the atomic doping by plasma techniques, remains challenging.

**Author Contributions:** F.Y., B.D. and L.Z. investigated and designed the review. M.L., C.M., and L.D. wrote the original draft preparation. F.Y., B.D., and L.Z. edited and reviewed the manuscript.

**Funding:** This research was funded the National Natural Science Foundation of China (21663022 and 21773020), the Program for Changjiang Scholars and Innovative Research Team in University (IRT\_15R46), and the Science and Technology Innovation Talents Program of Bingtuan (2019CB025).

**Conflicts of Interest:** The authors declare no competing financial interests.

## References

1. Seh, Z.W.; Kibsgaard, J.; Dickens, C.F.; Chorkendorff, I.; Nørskov, J.K.; Jaramillo, T.F. Combining theory and experiment in electrocatalysis: Insights into materials design. *Science* **2017**, *355*, eaad4998. [[CrossRef](#)] [[PubMed](#)]
2. Voiry, D.; Chhowalla, M.; Gogotsi, Y.; Kotov, N.A.; Li, Y.; Penner, R.M.; Schaak, R.E.; Weiss, P.S. Best Practices for Reporting Electrocatalytic Performance of Nanomaterials. *ACS Nano* **2018**, *12*, 9635–9638. [[CrossRef](#)] [[PubMed](#)]
3. Li, Q.; Rao, X.; Sheng, J.; Xu, J.; Yi, J.; Liu, Y.; Zhang, J. Energy storage through CO<sub>2</sub> electroreduction: A brief review of advanced Sn-based electrocatalysts and electrodes. *J. CO<sub>2</sub> Util.* **2018**, *27*, 48–59. [[CrossRef](#)]
4. Wang, Y.; Han, P.; Lv, X.; Zhang, L.; Zheng, G. Defect and Interface Engineering for Aqueous Electrocatalytic CO<sub>2</sub> Reduction. *Joule* **2018**, *2*, 2251–2587. [[CrossRef](#)]
5. Yan, D.F.; Li, Y.X.; Huo, J.; Chen, R.; Dai, L.M.; Wang, S.Y. Defect chemistry of nonprecious-metal electrocatalysts for oxygen reactions. *Adv. Mater.* **2017**, *29*, 1606459. [[CrossRef](#)] [[PubMed](#)]
6. Dou, S.; Wang, X.; Wang, S. Rational design of transition metal-based materials for highly efficient electrocatalysis. *Small Methods* **2018**, *3*, 1800211. [[CrossRef](#)]
7. Vogiatzis, K.D.; Polynski, M.V.; Kirkland, J.K.; Townsend, J.; Hashemi, A.; Liu, C.; Pidko, E.A. Computational approach to molecular catalysis by 3d transition metals: Challenges and opportunities. *Chem. Rev.* **2018**. [[CrossRef](#)] [[PubMed](#)]
8. Hong, W.T.; Risch, M.; Stoerzinger, K.A.; Grimaud, A.; Suntivich, J.; Shao-Horn, Y. Toward the rational design of non-precious transition metal oxides for oxygen electrocatalysis. *Energy Environ. Sci.* **2015**, *8*, 1404–1427. [[CrossRef](#)]
9. Liu, D.; Tao, L.; Yan, D.; Zou, Y.; Wang, S. Recent Advances on Non-precious Metal Porous Carbon-based Electrocatalysts for Oxygen Reduction Reaction. *ChemElectroChem* **2018**, *5*, 1775–1785. [[CrossRef](#)]
10. Wang, Z.; Zhang, Y.; Neyts, E.C.; Cao, X.; Zhang, X.; Jang, B.W.L.; Liu, C.-J. Catalyst Preparation with Plasmas: How Does It Work? *ACS Catal.* **2018**, *8*, 2093–2110. [[CrossRef](#)]
11. Liang, H.; Ming, F.; Alshareef, H.N. Applications of Plasma in Energy Conversion and Storage Materials. *Adv. Energy Mater.* **2018**. [[CrossRef](#)]
12. Keijsers, M.D.; Opdorp, C.V. Atomic layer epitaxy of gallium arsenide with the use of atomic hydrogen. *Appl. Phys. Lett.* **1991**, *58*, 1187–1189. [[CrossRef](#)]
13. Heil, S.B.S.; Hemmen, J.L.V.; Hodson, C.J.; Singh, N.; Klootwijk, J.H.; Roozeboom, F.; Sanden, M.C.M.V.D.; Kessels, W.M.M. Deposition of TiN and HfO<sub>2</sub> in a commercial 200mm remote plasma atomic layer deposition reactor. *J. Vac. Sci. Technol. A* **2007**, *25*, 1357–1366. [[CrossRef](#)]
14. Profijt, H.B.; Potts, S.E.; Sanden, M.C.M.V.D.; Kessels, W.M.M. Plasma-Assisted Atomic Layer Deposition: Basics, Opportunities, and Challenges. *J. Vac. Sci. Technol. A* **2011**, *29*, 050801. [[CrossRef](#)]
15. Ting, C.-C.; Liu, C.-H.; Tai, C.-Y.; Hsu, S.-C.; Chao, C.-S.; Pan, F.-M. The size effect of titania-supported Pt nanoparticles on the electrocatalytic activity towards methanol oxidation reaction primarily via the bifunctional mechanism. *J. Power Sources* **2015**, *280*, 166–172. [[CrossRef](#)]

16. Yoshiaki, A.; Hiroyuki, T.; Shigemitsu, T.; Satoshi, E.; Akihiro, T.; Narishi, G.; Victor, M.; Ali, A.; Saad, M.A.; Yuichiro, K.; et al. Preparation of a platinum electrocatalyst by coaxial pulse arc plasma deposition. *Sci. Technol. Adv. Mater.* **2015**, *16*, 024804.
17. Grigoriev, S.A.; Fedotov, A.A.; Martemianov, S.A.; Fateev, V.N. Synthesis of nanostructural electrocatalytic materials on various carbon substrates by ion plasma sputtering of platinum metals. *Russ. J. Electrochem.* **2014**, *50*, 638–646. [[CrossRef](#)]
18. Falch, A.; Lates, V.; Kriek, R.J. Combinatorial Plasma Sputtering of Pt<sub>x</sub>Pd<sub>y</sub> Thin Film Electrocatalysts for Aqueous SO<sub>2</sub> Electro-oxidation. *Electrocatalysis* **2015**, *6*, 322–330. [[CrossRef](#)]
19. Estevez, L.; Reed, D.; Nie, Z.; Schwarz, A.M.; Nandasiri, M.I.; Kizewski, J.P.; Wang, W.; Thomsen, E.; Liu, J.; Zhang, J.-G.; et al. Tunable Oxygen Functional Groups as Electrocatalysts on Graphite Felt Surfaces for All-Vanadium Flow Batteries. *ChemSusChem* **2016**, *9*, 1455–1461. [[CrossRef](#)]
20. Ma, Y.; Wang, Q.; Miao, Y.; Lin, Y.; Li, R. Plasma synthesis of Pt nanoparticles on 3D reduced graphene oxide-carbon nanotubes nanocomposites towards methanol oxidation reaction. *Appl. Surf. Sci.* **2018**, *450*, 413–421. [[CrossRef](#)]
21. Xu, J.L.; Wang, S.G.; Deng, Q.R.; Liu, Y.; Zhu, J.L.; Xu, C.B.; Wang, J.H. High-performance Pt/CNTs catalysts via hydrogen plasma for methanol electrooxidation. *Nano* **2014**, *9*, 1450018. [[CrossRef](#)]
22. Sui, S.; Ma, L.; Zhai, Y. TiC supported Pt–Ir electrocatalyst prepared by a plasma process for the oxygen electrode in unitized regenerative fuel cells. *J. Power Sources* **2011**, *196*, 5416–5422. [[CrossRef](#)]
23. Ipshita, B.; Kumaran, V.; Venugopal, S. Fabrication of electrodes with ultralow platinum loading by RF plasma processing of self-assembled arrays of Au@Pt nanoparticles. *Nanotechnology* **2016**, *27*, 305401.
24. Koh, J.H.; Jeon, H.S.; Jee, M.S.; Nursanto, E.B.; Lee, H.; Hwang, Y.J.; Min, B.K. Oxygen Plasma Induced Hierarchically Structured Gold Electrocatalyst for Selective Reduction of Carbon Dioxide to Carbon Monoxide. *J. Phys. Chem. C* **2015**, *119*, 883–889. [[CrossRef](#)]
25. Zhang, R.-C.; Sun, D.; Zhang, R.; Lin, W.-F.; Macias-Montero, M.; Patel, J.; Askari, S.; McDonald, C.; Mariotti, D.; Maguire, P. Gold nanoparticle-polymer nanocomposites synthesized by room temperature atmospheric pressure plasma and their potential for fuel cell electrocatalytic application. *Sci. Rep.* **2017**, *7*, 46682. [[CrossRef](#)]
26. Oi Lun, L.; Hoonseung, L.; Takahiro, I. Recent progress in solution plasma-synthesized-carbon-supported catalysts for energy conversion systems. *Jpn. J. Appl. Phys.* **2018**, *57*, 0102A2.
27. Kim, S.-M.; Cho, A.-R.; Lee, S.-Y. Characterization and electrocatalytic activity of Pt–M (M=Cu, Ag, and Pd) bimetallic nanoparticles synthesized by pulsed plasma discharge in water. *J. Nanopart. Res.* **2015**, *17*, 284. [[CrossRef](#)]
28. Kim, S.-M.; Lee, Y.-J.; Kim, J.-W.; Lee, S.-Y. Facile synthesis of Pt–Pd bimetallic nanoparticles by plasma discharge in liquid and their electrocatalytic activity toward methanol oxidation in alkaline media. *Thin Solid Films* **2014**, *572*, 260–265. [[CrossRef](#)]
29. Cho, A.-R.; Kim, S.-M.; Kim, S.-C.; Kim, J.-W.; Lee, S.-Y. The Facile Synthesis of Composition-Tunable Pt–Pd Bimetallic Nanocatalysts and Their Electrocatalytic Properties in Formic Acid. *J. Nanosci. Nanotechnol.* **2016**, *16*, 11443–11447. [[CrossRef](#)]
30. Zhang, J.; Hu, X.; Yang, B.; Su, N.; Huang, H.; Cheng, J.; Yang, H.; Saito, N. Novel synthesis of PtPd nanoparticles with good electrocatalytic activity and durability. *J. Alloy. Compd.* **2017**, *709*, 588–595. [[CrossRef](#)]
31. Horiguchi, G.; Chikaoka, Y.; Shiroishi, H.; Kosaka, S.; Saito, M.; Kameta, N.; Matsuda, N. Synthesis of Pt nanoparticles as catalysts of oxygen reduction with microbubble-assisted low-voltage and low-frequency solution plasma processing. *J. Power Sources* **2018**, *382*, 69–76. [[CrossRef](#)]
32. Huang, H.; Hu, X.; Zhang, J.; Su, N.; Cheng, J. Facile Fabrication of Platinum-Cobalt Alloy Nanoparticles with Enhanced Electrocatalytic Activity for a Methanol Oxidation Reaction. *Sci. Rep.* **2017**, *7*, 45555. [[CrossRef](#)] [[PubMed](#)]
33. Su, N.; Hu, X.; Zhang, J.; Huang, H.; Cheng, J.; Yu, J.; Ge, C. Plasma-induced synthesis of Pt nanoparticles supported on TiO<sub>2</sub> nanotubes for enhanced methanol electro-oxidation. *Appl. Surf. Sci.* **2017**, *399*, 403–410. [[CrossRef](#)]
34. Hu, X.; Shi, J.; Zhang, J.; Tang, W.; Zhu, H.; Shen, X.; Saito, N. One-step facile synthesis of carbon-supported PdAu nanoparticles and their electrochemical property and stability. *J. Alloy. Compd.* **2015**, *619*, 452–457. [[CrossRef](#)]

35. Kang, J.; Li, O.L.; Saito, N. A simple synthesis method for nano-metal catalyst supported on mesoporous carbon: The solution plasma process. *Nanoscale* **2013**, *5*, 6874–6882. [[CrossRef](#)] [[PubMed](#)]
36. Kang, J.; Saito, N. In situ solution plasma synthesis of mesoporous nanocarbon-supported bimetallic nanoparticles. *RSC Adv.* **2015**, *5*, 29131–29134. [[CrossRef](#)]
37. Sung-Min, K.; Sang-Yul, L. The plasma-induced formation of silver nanocrystals in aqueous solution and their catalytic activity for oxygen reduction. *Nanotechnology* **2018**, *29*, 085602.
38. Lee, Y.-J.; Kim, S.-M.; Kim, J.-W.; Lee, S.-Y. The characterization and electrocatalytic activities of carbon-supported Pt nanoparticles synthesized by the solution plasma process. *Mater. Lett.* **2014**, *123*, 184–186. [[CrossRef](#)]
39. Hussain, S.; Erikson, H.; Kongi, N.; Treshchalov, A.; Rähn, M.; Kook, M.; Merisalu, M.; Matisen, L.; Sammelselg, V.; Tammeveski, K. Oxygen Electroreduction on Pt Nanoparticles Deposited on Reduced Graphene Oxide and N-doped Reduced Graphene Oxide Prepared by Plasma-assisted Synthesis in Aqueous Solution. *ChemElectroChem* **2018**, *5*, 2902–2911. [[CrossRef](#)]
40. Cui, B.; Hu, B.; Liu, J.; Wang, M.; Song, Y.; Tian, K.; Zhang, Z.; He, L. Solution-Plasma-Assisted Bimetallic Oxide Alloy Nanoparticles of Pt and Pd Embedded within Two-Dimensional  $Ti_3C_2T_x$  Nanosheets as Highly Active Electrocatalysts for Overall Water Splitting. *ACS Appl. Mater. Interfaces* **2018**, *10*, 23858–23873. [[CrossRef](#)]
41. Huang, H.; Liu, Y.; Ma, X.; Hu, J. Silver nanoparticles supported on graphitization micro-diamond as an electrocatalyst in alkaline medium. *Vacuum* **2018**, *155*, 380–386. [[CrossRef](#)]
42. Ding, G.; Jiao, W.; Wang, R.; Niu, Y.; Chen, L.; Hao, L. Ultrafast, Reversible Transition of Superwettability of Graphene Network and Controllable Underwater Oil Adhesion for Oil Microdroplet Transportation. *Adv. Funct. Mater.* **2018**, *28*, 1706686. [[CrossRef](#)]
43. Li, J.; Chen, G.; Zhu, Y.; Liang, Z.; Pei, A.; Wu, C.-L.; Wang, H.; Lee, H.R.; Liu, K.; Chu, S.; et al. Efficient electrocatalytic  $CO_2$  reduction on a three-phase interface. *Nat. Catal.* **2018**, *1*, 592–600. [[CrossRef](#)]
44. Chetty, R.; Maniam, K.K.; Schuhmann, W.; Muhler, M. Oxygen-Plasma-Functionalized Carbon Nanotubes as Supports for Platinum–Ruthenium Catalysts Applied in Electrochemical Methanol Oxidation. *ChemPlusChem* **2015**, *80*, 130–135. [[CrossRef](#)]
45. Ding, D.; Song, Z.-L.; Cheng, Z.-Q.; Liu, W.-N.; Nie, X.-K.; Bian, X.; Chen, Z.; Tan, W. Plasma-assisted nitrogen doping of graphene-encapsulated Pt nanocrystals as efficient fuel cell catalysts. *J. Mater. Chem. A* **2014**, *2*, 472–477. [[CrossRef](#)]
46. Loganathan, K.; Bose, D.; Weinkauf, D. Surface modification of carbon black by nitrogen and allylamine plasma treatment for fuel cell electrocatalyst. *Int. J. Hydrogen Energy* **2014**, *39*, 15766–15771. [[CrossRef](#)]
47. Du, S.; Lin, K.; Malladi, S.K.; Lu, Y.; Sun, S.; Xu, Q.; Steinberger-Wilckens, R.; Dong, H. Plasma nitriding induced growth of Pt-nanowire arrays as high performance electrocatalysts for fuel cells. *Sci. Rep.* **2014**, *4*, 6439. [[CrossRef](#)]
48. Hu, X.; Ge, C.; Su, N.; Huang, H.; Xu, Y.; Zhang, J.; Shi, J.; Shen, X.; Saito, N. Solution plasma synthesis of Pt/ZnO/KB for photo-assisted electro-oxidation of methanol. *J. Alloy. Compd.* **2017**, *692*, 848–854. [[CrossRef](#)]
49. Flis-Kabulska, I.; Sun, Y.; Zakroczymski, T.; Flis, J. Plasma carburizing for improvement of Ni-Fe cathodes for alkaline water electrolysis. *Electrochim. Acta* **2016**, *220*, 11–19. [[CrossRef](#)]
50. Jin, Q.; Ren, B.; Li, D.; Cui, H.; Wang, C. Plasma-Assisted Synthesis of Self-Supporting Porous CoNPs@C Nanosheet as Efficient and Stable Bifunctional Electrocatalysts for Overall Water Splitting. *ACS Appl. Mater. Interfaces* **2017**, *9*, 31913–31921. [[CrossRef](#)]
51. Koo, Y.; Malik, R.; Alvarez, N.; White, L.; Shanov, V.N.; Schulz, M.; Collins, B.; Sankar, J.; Yun, Y. Aligned carbon nanotube/copper sheets: A new electrocatalyst for  $CO_2$  reduction to hydrocarbons. *RSC Adv.* **2014**, *4*, 16362–16367. [[CrossRef](#)]
52. Mistry, H.; Varela, A.S.; Bonifacio, C.S.; Zegkinoglou, I.; Sinev, I.; Choi, Y.-W.; Kisslinger, K.; Stach, E.A.; Yang, J.C.; Strasser, P.; et al. Highly selective plasma-activated copper catalysts for carbon dioxide reduction to ethylene. *Nat. Commun.* **2016**, *7*, 12123. [[CrossRef](#)]
53. Gao, D.; Zegkinoglou, I.; Divins, N.J.; Scholten, F.; Sinev, I.; Grosse, P.; Roldan Cuenya, B. Plasma-Activated Copper Nanocube Catalysts for Efficient Carbon Dioxide Electroreduction to Hydrocarbons and Alcohols. *ACS Nano* **2017**, *11*, 4825–4831. [[CrossRef](#)] [[PubMed](#)]

54. Zhang, R.; Zhang, Y.-C.; Pan, L.; Shen, G.-Q.; Mahmood, N.; Ma, Y.-H.; Shi, Y.; Jia, W.; Wang, L.; Zhang, X.; et al. Engineering Cobalt Defects in Cobalt Oxide for Highly Efficient Electrocatalytic Oxygen Evolution. *ACS Catal.* **2018**, *8*, 3803–3811. [[CrossRef](#)]
55. Jozwiak, L.; Balcerzak, J.; Kubiczek, A.; Tyczkowski, J. Plasma deposited thin-film sandwich-like bifunctional electrocatalyst for oxygen reduction and evolution reactions. *Thin Solid Films* **2018**, *660*, 161–165. [[CrossRef](#)]
56. Kim, S.-M.; Jo, Y.-G.; Lee, M.-H.; Saito, N.; Kim, J.-W.; Lee, S.-Y. The plasma-assisted formation of Ag@Co<sub>3</sub>O<sub>4</sub> core-shell hybrid nanocrystals for oxygen reduction reaction. *Electrochim. Acta* **2017**, *233*, 123–133. [[CrossRef](#)]
57. Taiwo, O.; Jun, M.; Yi, G.; Wei, Z.; Jian, J.; Zhao, X.S.; Zhonghua, Z. A new approach to nanoporous graphene sheets via rapid microwave-induced plasma for energy applications. *Nanotechnology* **2014**, *25*, 495604.
58. Lang, X.; Zhang, Y.; Cai, K.; Li, L.; Wang, Q.; Zhang, Q. High performance CoO nanospheres catalyst synthesized by DC arc discharge plasma method as air electrode for lithium-oxygen battery. *Ionics* **2018**, *25*, 35–40. [[CrossRef](#)]
59. Gan, Q.; He, H.; Zhao, K.; He, Z.; Liu, S.; Yang, S. Plasma-Induced Oxygen Vacancies in Urchin-Like Anatase Titania Coated by Carbon for Excellent Sodium-Ion Battery Anodes. *ACS Appl. Mater. Interfaces* **2018**, *10*, 7031–7042. [[CrossRef](#)]
60. Xu, L.; Jiang, Q.; Xiao, Z.; Li, X.; Huo, J.; Wang, S.; Dai, L. Plasma-Engraved Co<sub>3</sub>O<sub>4</sub> Nanosheets with Oxygen Vacancies and High Surface Area for the Oxygen Evolution Reaction. *Angew. Chem. Int. Ed.* **2016**, *55*, 5277–5281. [[CrossRef](#)]
61. Wang, J.; Liu, J.; Zhang, B.; Wan, H.; Li, Z.; Ji, X.; Xu, K.; Chen, C.; Zha, D.; Miao, L.; et al. Synergistic effect of two actions sites on cobalt oxides towards electrochemical water-oxidation. *Nano Energy* **2017**, *42*, 98–105. [[CrossRef](#)]
62. Ma, L.; Chen, S.; Pei, Z.; Li, H.; Wang, Z.; Liu, Z.; Tang, Z.; Zapfen, J.A.; Zhi, C. Flexible Waterproof Rechargeable Hybrid Zinc Batteries Initiated by Multifunctional Oxygen Vacancies-Rich Cobalt Oxide. *ACS Nano* **2018**, *12*, 8597–8605. [[CrossRef](#)] [[PubMed](#)]
63. Min, W. Plasma-induced nanoporous metal oxides with nitrogen doping for high-performance electrocatalysis. *Nanotechnology* **2017**, *28*, 242501.
64. Lei, X.; Zhimin, W.; Jialu, W.; Zhaohui, X.; Xiaobing, H.; Zhigang, L.; Shuangyin, W. N-doped nanoporous Co<sub>3</sub>O<sub>4</sub> nanosheets with oxygen vacancies as oxygen evolving electrocatalysts. *Nanotechnology* **2017**, *28*, 165402.
65. Uhlig, L.M.; Sievers, G.; Brüser, V.; Dyck, A.; Wittstock, G. Characterization of different plasma-treated cobalt oxide catalysts for oxygen reduction reaction in alkaline media. *Sci. Bull.* **2016**, *61*, 612–618. [[CrossRef](#)]
66. Liang, H.; Xia, C.; Emwas, A.-H.; Anjum, D.H.; Miao, X.; Alshareef, H.N. Phosphine plasma activation of  $\alpha$ -Fe<sub>2</sub>O<sub>3</sub> for high energy asymmetric supercapacitors. *Nano Energy* **2018**, *49*, 155–162. [[CrossRef](#)]
67. Xiao, Z.H.; Wang, Y.; Huang, Y.C.; Wei, Z.X.; Dong, C.L.; Ma, J.M.; Shen, S.H.; Li, Y.F.; Wang, S.Y. Filling the oxygen vacancies in Co<sub>3</sub>O<sub>4</sub> with phosphorus: An ultra-efficient electrocatalyst for overall water splitting. *Energy Environ. Sci.* **2017**, *10*, 2563–2569. [[CrossRef](#)]
68. Wang, Z.; Liu, H.; Ge, R.; Ren, X.; Ren, J.; Yang, D.; Zhang, L.; Sun, X. Phosphorus-Doped Co<sub>3</sub>O<sub>4</sub> Nanowire Array: A Highly Efficient Bifunctional Electrocatalyst for Overall Water Splitting. *ACS Catal.* **2018**, *8*, 2236–2241. [[CrossRef](#)]
69. Dou, S.; Dong, C.-L.; Hu, Z.; Huang, Y.-C.; Chen, J.-I.; Tao, L.; Yan, D.; Chen, D.; Shen, S.; Chou, S.; et al. Atomic-Scale CoO<sub>x</sub> Species in Metal–Organic Frameworks for Oxygen Evolution Reaction. *Adv. Funct. Mater.* **2017**, *27*, 1702546. [[CrossRef](#)]
70. Yin, W.-J.; Weng, B.; Ge, J.; Sun, Q.; Li, Z.; Yan, Y. Oxide perovskites, double perovskites and derivatives for electrocatalysis, photocatalysis, and photovoltaics. *Energy Environ. Sci.* **2018**, *12*, 442–462. [[CrossRef](#)]
71. Chen, D.; Qiao, M.; Lu, Y.-R.; Hao, L.; Liu, D.; Dong, C.-L.; Li, Y.; Wang, S. Preferential Cation Vacancies in Perovskite Hydroxide for the Oxygen Evolution Reaction. *Angew. Chem. Int. Ed.* **2018**, *57*, 8691–8696. [[CrossRef](#)] [[PubMed](#)]
72. Hayden, B.E.; Rogers, F.K. Oxygen reduction and oxygen evolution on SrTi<sub>1-x</sub>Fe<sub>x</sub>O<sub>3-y</sub> (STFO) perovskite electrocatalysts. *J. Electroanal. Chem.* **2018**, *819*, 275–282. [[CrossRef](#)]
73. Chen, G.; Hu, Z.; Zhu, Y.; Gu, B.; Zhong, Y.; Lin, H.-J.; Chen, C.-T.; Zhou, W.; Shao, Z. A Universal Strategy to Design Superior Water-Splitting Electrocatalysts Based on Fast In Situ Reconstruction of Amorphous Nanofilm Precursors. *Adv. Mater.* **2018**, *30*, 1804333. [[CrossRef](#)] [[PubMed](#)]

74. Liu, R.; Wang, Y.Y.; Liu, D.D.; Zou, Y.Q.; Wang, S.Y. Water-Plasma-Enabled Exfoliation of Ultrathin Layered Double Hydroxide Nanosheets with Multivacancies for Water Oxidation. *Adv. Mater.* **2017**, *29*, 1701546. [[CrossRef](#)] [[PubMed](#)]
75. Carrasco, J.A.; Romero, J.; Varela, M.; Hauke, F.; Abellán, G.; Hirsch, A.; Coronado, E. Alkoxide-intercalated NiFe-layered double hydroxides magnetic nanosheets as efficient water oxidation electrocatalysts. *Inorg. Chem. Front.* **2016**, *3*, 478–487. [[CrossRef](#)]
76. Browne, M.P.; Sofer, Z.; Pumera, M. Layered and two dimensional metal oxides for electrochemical energy conversion. *Energy Environ. Sci.* **2018**, *12*, 41–58. [[CrossRef](#)]
77. Wang, Y.Y.; Zhang, Y.Q.; Liu, Z.J.; Xie, C.; Feng, S.; Liu, D.D.; Shao, M.F.; Wang, S.Y. Layered double hydroxide nanosheets with multiple vacancies obtained by dry exfoliation as highly efficient oxygen evolution electrocatalysts. *Angew. Chem. Int. Ed.* **2017**, *56*, 5867–5871. [[CrossRef](#)] [[PubMed](#)]
78. Wang, Y.Y.; Xie, C.; Zhang, Z.Y.; Liu, D.D.; Chen, R.; Wang, S.Y. In Situ Exfoliated, N-Doped, and Edge-Rich Ultrathin Layered Double Hydroxides Nanosheets for Oxygen Evolution Reaction. *Adv. Funct. Mater.* **2018**, *28*, 1703363. [[CrossRef](#)]
79. Oturan, N.; Ganiyu, S.O.; Raffy, S.; Oturan, M.A. Sub-stoichiometric titanium oxide as a new anode material for electro-Fenton process: Application to electrocatalytic destruction of antibiotic amoxicillin. *Appl. Catal. B Environ.* **2017**, *217*, 214–223. [[CrossRef](#)]
80. Luo, X.; Lu, J.; Sohm, E.; Ma, L.; Wu, T.; Wen, J.; Qiu, D.; Xu, Y.; Ren, Y.; Miller, D.J.; et al. Uniformly dispersed FeO<sub>x</sub> atomic clusters by pulsed arc plasma deposition: An efficient electrocatalyst for improving the performance of Li–O<sub>2</sub> battery. *Nano Res.* **2016**, *9*, 1913–1920. [[CrossRef](#)]
81. Peng, X.; Wang, Z.; Wang, Z.; Pan, Y. Multivalent manganese oxides with high electrocatalytic activity for oxygen reduction reaction. *Front. Chem. Sci. Eng.* **2018**, *12*, 790–797. [[CrossRef](#)]
82. Jiang, M.; Fu, C.; Yang, J.; Liu, Q.; Zhang, J.; Sun, B. Defect-engineered MnO<sub>2</sub> enhancing oxygen reduction reaction for high performance Al-air batteries. *Energy Storage Mater.* **2018**, *18*, 34–42. [[CrossRef](#)]
83. Zhang, Y.; Ouyang, B.; Xu, K.; Xia, X.; Zhang, Z.; Rawat, R.S.; Fan, H.J. Prereduction of Metal Oxides via Carbon Plasma Treatment for Efficient and Stable Electrocatalytic Hydrogen Evolution. *Small* **2018**, *14*, 1800340. [[CrossRef](#)] [[PubMed](#)]
84. Geng, Z.; Kong, X.; Chen, W.; Su, H.; Liu, Y.; Cai, F.; Wang, G.; Zeng, J. Oxygen Vacancies in ZnO Nanosheets Enhance CO<sub>2</sub> Electrochemical Reduction to CO. *Angew. Chem. Int. Ed.* **2018**, *57*, 6054–6059. [[CrossRef](#)] [[PubMed](#)]
85. Li, H.; Tan, Y.; Liu, P.; Guo, C.; Luo, M.; Han, J.; Lin, T.; Huang, F.; Chen, M. Atomic-Sized Pores Enhanced Electrocatalysis of TaS<sub>2</sub> Nanosheets for Hydrogen Evolution. *Adv. Mater.* **2016**, *28*, 8945–8949. [[CrossRef](#)] [[PubMed](#)]
86. Tao, L.; Duan, X.; Wang, C.; Duan, X.; Wang, S. Plasma-engineered MoS<sub>2</sub> thin-film as an efficient electrocatalyst for hydrogen evolution reaction. *Chem. Commun.* **2015**, *51*, 7470–7473. [[CrossRef](#)]
87. Zhang, C.; Jiang, L.; Zhang, Y.; Hu, J.; Leung, M.K.H. Janus effect of O<sub>2</sub> plasma modification on the electrocatalytic hydrogen evolution reaction of MoS<sub>2</sub>. *J. Catal.* **2018**, *361*, 384–392. [[CrossRef](#)]
88. Huang, J.; Deng, X.; Wan, H.; Chen, F.; Lin, Y.; Xu, X.; Ma, R.; Sasaki, T. Liquid Phase Exfoliation of MoS<sub>2</sub> Assisted by Formamide Solvothermal Treatment and Enhanced Electrocatalytic Activity Based on (H<sub>3</sub>Mo<sub>12</sub>O<sub>40</sub>P/MoS<sub>2</sub>)<sub>n</sub> Multilayer Structure. *ACS Sustain. Chem. Eng.* **2018**, *6*, 5227–5237. [[CrossRef](#)]
89. Cheng, C.-C.; Lu, A.-Y.; Tseng, C.-C.; Yang, X.; Hedhili, M.N.; Chen, M.-C.; Wei, K.-H.; Li, L.-J. Activating basal-plane catalytic activity of two-dimensional MoS<sub>2</sub> monolayer with remote hydrogen plasma. *Nano Energy* **2016**, *30*, 846–852. [[CrossRef](#)]
90. Lu, A.-Y.; Yang, X.; Tseng, C.-C.; Min, S.; Lin, S.-H.; Hsu, C.-L.; Li, H.; Idriss, H.; Kuo, J.-L.; Huang, K.-W.; et al. High-Sulfur-Vacancy Amorphous Molybdenum Sulfide as a High Current Electrocatalyst in Hydrogen Evolution. *Small* **2016**, *12*, 5530–5537. [[CrossRef](#)]
91. Dou, S.; Tao, L.; Huo, J.; Wang, S.; Dai, L. Etched and doped Co<sub>9</sub>S<sub>8</sub>/graphene hybrid for oxygen electrocatalysis. *Energy Environ. Sci.* **2016**, *9*, 1320–1326. [[CrossRef](#)]
92. Zhang, C.; Shi, Y.; Yu, Y.; Du, Y.; Zhang, B. Engineering Sulfur Defects, Atomic Thickness, and Porous Structures into Cobalt Sulfide Nanosheets for Efficient Electrocatalytic Alkaline Hydrogen Evolution. *ACS Catal.* **2018**, *8*, 8077–8083. [[CrossRef](#)]

93. He, L.; Zhou, D.; Lin, Y.; Ge, R.; Hou, X.; Sun, X.; Zheng, C. Ultrarapid in Situ Synthesis of Cu<sub>2</sub>S Nanosheet Arrays on Copper Foam with Room-Temperature-Active Iodine Plasma for Efficient and Cost-Effective Oxygen Evolution. *ACS Catal.* **2018**, *8*, 3859–3864. [[CrossRef](#)]
94. Yeo, S.; Nandi, D.K.; Rahul, R.; Kim, T.H.; Shong, B.; Jang, Y.; Bae, J.-S.; Han, J.W.; Kim, S.-H.; Kim, H. Low-temperature direct synthesis of high quality WS<sub>2</sub> thin films by plasma-enhanced atomic layer deposition for energy related applications. *Appl. Surf. Sci.* **2018**, *459*, 596–605. [[CrossRef](#)]
95. Escalera-López, D.; Griffin, R.; Isaacs, M.; Wilson, K.; Palmer, R.E.; Rees, N.V. MoS<sub>2</sub> and WS<sub>2</sub> nanocone arrays: Impact of surface topography on the hydrogen evolution electrocatalytic activity and mass transport. *Appl. Mater. Today* **2018**, *11*, 70–81. [[CrossRef](#)]
96. Qu, S.; Chen, W.; Yu, J.; Chen, G.; Zhang, R.; Chu, S.; Huang, J.; Wang, X.; Li, C.; Ostrikov, K. Cross-linked trimetallic nanopetals for electrocatalytic water splitting. *J. Power Sources* **2018**, *390*, 224–233. [[CrossRef](#)]
97. Sun, Y.; Xu, K.; Wei, Z.; Li, H.; Zhang, T.; Li, X.; Cai, W.; Ma, J.; Fan, H.J.; Li, Y. Strong Electronic Interaction in Dual-Cation-Incorporated NiSe<sub>2</sub> Nanosheets with Lattice Distortion for Highly Efficient Overall Water Splitting. *Adv. Mater.* **2018**, *30*, 1802121. [[CrossRef](#)]
98. Deng, S.; Zhong, Y.; Zeng, Y.; Wang, Y.; Yao, Z.; Yang, F.; Lin, S.; Wang, X.; Lu, X.; Xia, X.; et al. Directional Construction of Vertical Nitrogen-Doped 1T-2H MoSe<sub>2</sub>/Graphene Shell/Core Nanoflake Arrays for Efficient Hydrogen Evolution Reaction. *Adv. Mater.* **2017**, *29*, 1700748. [[CrossRef](#)]
99. Li, Y.; Liu, J.; Yuan, Q.; Tang, H.; Yu, F.; Lv, X. A green adsorbent derived from banana peel for highly effective removal of heavy metal ions from water. *RSC Adv.* **2016**, *6*, 45041–45048. [[CrossRef](#)]
100. Zhang, Y.; Ouyang, B.; Xu, J.; Chen, S.; Rawat, R.S.; Fan, H.J. 3D Porous Hierarchical Nickel–Molybdenum Nitrides Synthesized by RF Plasma as Highly Active and Stable Hydrogen-Evolution-Reaction Electrocatalysts. *Adv. Energy Mater.* **2016**, *6*, 1600221. [[CrossRef](#)]
101. Ouyang, B.; Zhang, Y.; Zhang, Z.; Fan, H.J.; Rawat, R.S. Nitrogen-Plasma-Activated Hierarchical Nickel Nitride Nanocorals for Energy Applications. *Small* **2017**, *13*, 1604265. [[CrossRef](#)] [[PubMed](#)]
102. Liu, B.; He, B.; Peng, H.-Q.; Zhao, Y.; Cheng, J.; Xia, J.; Shen, J.; Ng, T.-W.; Meng, X.; Lee, C.-S.; et al. Unconventional Nickel Nitride Enriched with Nitrogen Vacancies as a High-Efficiency Electrocatalyst for Hydrogen Evolution. *Adv. Sci.* **2018**, *5*, 1800406. [[CrossRef](#)] [[PubMed](#)]
103. Wang, L.-C.; Liu, B.-H.; Su, C.-Y.; Liu, W.-S.; Kei, C.-C.; Wang, K.-W.; Perng, T.-P. Electronic Band Structure and Electrocatalytic Performance of Cu<sub>3</sub>N Nanocrystals. *ACS Appl. Nano Mater.* **2018**, *1*, 3673–3681. [[CrossRef](#)]
104. Panomsuwan, G.; Saito, N.; Ishizaki, T. Fe–N-doped carbon-based composite as an efficient and durable electrocatalyst for the oxygen reduction reaction. *RSC Adv.* **2016**, *6*, 114553–114559. [[CrossRef](#)]
105. Zhong, W.; Chen, J.; Zhang, P.; Deng, L.; Yao, L.; Ren, X.; Li, Y.; Mi, H.; Sun, L. Air plasma etching towards rich active sites in Fe/N-porous carbon for the oxygen reduction reaction with superior catalytic performance. *J. Mater. Chem. A* **2017**, *5*, 16605–16610. [[CrossRef](#)]
106. Wu, R.; Xiao, B.; Gao, Q.; Zheng, Y.-R.; Zheng, X.-S.; Zhu, J.-F.; Gao, M.-R.; Yu, S.-H. A Janus Nickel Cobalt Phosphide Catalyst for High-Efficiency Neutral-pH Water Splitting. *Angew. Chem. Int. Ed.* **2018**, *57*, 15445–15449. [[CrossRef](#)]
107. Pan, Y.; Sun, K.; Lin, Y.; Cao, X.; Cheng, Y.; Liu, S.; Zeng, L.; Cheong, W.-C.; Zhao, D.; Wu, K.; et al. Electronic structure and d-band center control engineering over M-doped CoP (M=Ni, Mn, Fe) hollow polyhedron frames for boosting hydrogen production. *Nano Energy* **2019**, *56*, 411–419. [[CrossRef](#)]
108. Liang, H.; Gandhi, A.N.; Anjum, D.H.; Wang, X.; Schwingenschlögl, U.; Alshareef, H.N. Plasma-Assisted Synthesis of NiCoP for Efficient Overall Water Splitting. *Nano Lett.* **2016**, *16*, 7718–7725. [[CrossRef](#)]
109. Zhang, Q.; Li, T.; Liang, J.; Wang, N.; Kong, X.; Wang, J.; Qian, H.; Zhou, Y.; Liu, F.; Wei, C.; et al. Highly wettable and metallic NiFe-phosphate/phosphide catalyst synthesized by plasma for highly efficient oxygen evolution reaction. *J. Mater. Chem. A* **2018**, *6*, 7509–7516. [[CrossRef](#)]
110. Dinh, K.N.; Sun, X.; Dai, Z.; Zheng, Y.; Zheng, P.; Yang, J.; Xu, J.; Wang, Z.; Yan, Q. O<sub>2</sub> plasma and cation tuned nickel phosphide nanosheets for highly efficient overall water splitting. *Nano Energy* **2018**, *54*, 82–90. [[CrossRef](#)]
111. Peng, X.; Qasim, A.M.; Jin, W.; Wang, L.; Hu, L.; Miao, Y.; Li, W.; Li, Y.; Liu, Z.; Huo, K.; et al. Ni-doped amorphous iron phosphide nanoparticles on TiN nanowire arrays: An advanced alkaline hydrogen evolution electrocatalyst. *Nano Energy* **2018**, *53*, 66–73. [[CrossRef](#)]

112. Goryachev, A.; Gao, L.; Zhang, Y.; Rohling, R.Y.; Vervuurt, R.H.J.; Bol, A.A.; Hofmann, J.P.; Hensen, E.J.M. Stability of CoP<sub>x</sub> Electrocatalysts in Continuous and Interrupted Acidic Electrolysis of Water. *ChemElectroChem* **2018**, *5*, 1230–1239. [[CrossRef](#)] [[PubMed](#)]
113. Liu, H.; Liu, X.; Mao, Z.; Zhao, Z.; Peng, X.; Luo, J.; Sun, X. Plasma-activated Co<sub>3</sub>(PO<sub>4</sub>)<sub>2</sub> nanosheet arrays with Co<sup>3+</sup>-Rich surfaces for overall water splitting. *J. Power Sources* **2018**, *400*, 190–197. [[CrossRef](#)]
114. Guo, Q.; Guo, Z.; Shi, J.; Xiong, W.; Zhang, H.; Chen, Q.; Liu, Z.; Wang, X. Atomic Layer Deposition of Nickel Carbide from a Nickel Amidinate Precursor and Hydrogen Plasma. *ACS Appl. Mater. Interfaces* **2018**, *10*, 8384–8390. [[CrossRef](#)] [[PubMed](#)]
115. Xiong, W.; Guo, Q.; Guo, Z.; Li, H.; Zhao, R.; Chen, Q.; Liu, Z.; Wang, X. Atomic layer deposition of nickel carbide for supercapacitors and electrocatalytic hydrogen evolution. *J. Mater. Chem. A* **2018**, *6*, 4297–4304. [[CrossRef](#)]
116. Ko, Y.-J.; Cho, J.-M.; Kim, I.; Jeong, D.S.; Lee, K.-S.; Park, J.-K.; Baik, Y.-J.; Choi, H.-J.; Lee, W.-S. Tungsten carbide nanowalls as electrocatalyst for hydrogen evolution reaction: New approach to durability issue. *Appl. Catal. B Environ.* **2017**, *203*, 684–691. [[CrossRef](#)]
117. Guo, Y.; Teng, W.; Chen, J.; Jie, Z.; Ostrikov, K.K. Air Plasma Activation of Catalytic Sites in a Metal-Cyanide Framework for Efficient Oxygen Evolution Reaction. *Adv. Energy Mater.* **2018**, *8*, 1800085. [[CrossRef](#)]
118. Yan, D.; Dong, C.-L.; Huang, Y.-C.; Zou, Y.; Xie, C.; Wang, Y.; Zhang, Y.; Liu, D.; Shen, S.; Wang, S. Engineering the coordination geometry of metal–organic complex electrocatalysts for highly enhanced oxygen evolution reaction. *J. Mater. Chem. A* **2018**, *6*, 805–810. [[CrossRef](#)]
119. Ghausi, M.A.; Xie, J.; Li, Q.; Wang, X.; Yang, R.; Wu, M.; Wang, Y.; Dai, L. CO<sub>2</sub> Overall Splitting by a Bifunctional Metal-Free Electrocatalyst. *Angew. Chem. Int. Ed.* **2018**, *57*, 13135–13139. [[CrossRef](#)]
120. Lai, J.; Nsabimana, A.; Luque, R.; Xu, G. 3D Porous Carbonaceous Electrodes for Electrocatalytic Applications. *Joule* **2018**, *2*, 76–93. [[CrossRef](#)]
121. Liu, M.; Yu, F.; Ma, C.; Xue, X.; Fu, H.; Yuan, H.; Yang, S.; Wang, G.; Guo, X.; Zhang, L. Effective Oxygen Reduction Reaction Performance of FeCo Alloys In Situ Anchored on Nitrogen-Doped Carbon by the Microwave-Assistant Carbon Bath Method and Subsequent Plasma Etching. *Nanomaterials* **2019**, *9*, 1284. [[CrossRef](#)] [[PubMed](#)]
122. Hong, J.; Jin, C.; Yuan, J.; Zhang, Z. Atomic Defects in Two-Dimensional Materials: From Single-Atom Spectroscopy to Functionalities in Opto-/Electronics, Nanomagnetism, and Catalysis. *Adv. Mater.* **2017**, *29*, 1606434. [[CrossRef](#)] [[PubMed](#)]
123. Jiang, H.; Gu, J.; Zheng, X.; Liu, M.; Qiu, X.; Wang, L.; Li, W.; Chen, Z.; Ji, X.; Li, J. Defect-rich and ultrathin N doped carbon nanosheets as advanced trifunctional metal-free electrocatalysts for ORR, OER and HER. *Energy Environ. Sci.* **2019**, *12*, 322–333. [[CrossRef](#)]
124. Tao, L.; Wang, Q.; Dou, S.; Ma, Z.L.; Huo, J.; Wang, S.Y.; Dai, L.M. Edge-rich and dopant-free graphene as a highly efficient metal-free electrocatalyst for the oxygen reduction reaction. *Chem. Commun.* **2016**, *52*, 2764–2767. [[CrossRef](#)] [[PubMed](#)]
125. Liu, Z.J.; Zhao, Z.H.; Wang, Y.Y.; Dou, S.; Yan, D.F.; Liu, D.D.; Xia, Z.H.; Wang, S.Y. In Situ Exfoliated, Edge-Rich, Oxygen-Functionalized Graphene from Carbon Fibers for Oxygen Electrocatalysis. *Adv. Mater.* **2017**, *29*, 1606207. [[CrossRef](#)] [[PubMed](#)]
126. Lehmann, K.; Yurchenko, O.; Melke, J.; Fischer, A.; Urban, G. High electrocatalytic activity of metal-free and non-doped hierarchical carbon nanowalls towards oxygen reduction reaction. *Electrochim. Acta* **2018**, *269*, 657–667. [[CrossRef](#)]
127. Wang, Y.; Yu, F.; Zhu, M.; Ma, C.; Zhao, D.; Wang, C.; Zhou, A.; Dai, B.; Ji, J.; Guo, X. N-Doping of plasma exfoliated graphene oxide via dielectric barrier discharge plasma treatment for the oxygen reduction reaction. *J. Mater. Chem. A* **2018**, *6*, 2011–2017. [[CrossRef](#)]
128. Zhu, Y.-P.; Ran, J.; Qiao, S.-Z. Scalable Self-Supported Graphene Foam for High-Performance Electrocatalytic Oxygen Evolution. *ACS Appl. Mater. Interfaces* **2017**, *9*, 41980–41987. [[CrossRef](#)]
129. Yu, D.; Zhang, Q.; Dai, L. Highly Efficient Metal-Free Growth of Nitrogen-Doped Single-Walled Carbon Nanotubes on Plasma-Etched Substrates for Oxygen Reduction. *J. Am. Chem. Soc.* **2010**, *132*, 15127–15129. [[CrossRef](#)]
130. Du, Z.; Wang, S.; Kong, C.; Deng, Q.; Wang, G.; Liang, C.; Tang, H. Microwave plasma synthesized nitrogen-doped carbon nanotubes for oxygen reduction. *J. Solid State Electrochem.* **2015**, *19*, 1541–1549. [[CrossRef](#)]



131. Subramanian, P.; Cohen, A.; Teblum, E.; Nessim, G.D.; Bormasheko, E.; Schechter, A. Electrocatalytic activity of nitrogen plasma treated vertically aligned carbon nanotube carpets towards oxygen reduction reaction. *Electrochem. Commun.* **2014**, *49*, 42–46. [[CrossRef](#)]
132. Zhang, S.; Kang, P.; Ubnoske, S.; Brennaman, M.K.; Song, N.; House, R.L.; Glass, J.T.; Meyer, T.J. Polyethylenimine-Enhanced Electrocatalytic Reduction of CO<sub>2</sub> to Formate at Nitrogen-Doped Carbon Nanomaterials. *J. Am. Chem. Soc.* **2014**, *136*, 7845–7848. [[CrossRef](#)] [[PubMed](#)]
133. Li, O.L.; Wada, Y.; Kaneko, A.; Lee, H.; Ishizaki, T. Oxygen Reduction Reaction Activity of Thermally Tailored Nitrogen-Doped Carbon Electrocatalysts Prepared through Plasma Synthesis. *ChemElectroChem* **2018**, *5*, 1995–2001. [[CrossRef](#)]
134. Hyun, K.; Ueno, T.; Li, O.L.; Saito, N. Synthesis of heteroatom-carbon nanosheets by solution plasma processing using N-methyl-2-pyrrolidone as precursor. *RSC Adv.* **2016**, *6*, 6990–6996. [[CrossRef](#)]
135. Li, O.L.; Chiba, S.; Wada, Y.; Panomsuwan, G.; Ishizaki, T. Synthesis of graphitic-N and amino-N in nitrogen-doped carbon via a solution plasma process and exploration of their synergic effect for advanced oxygen reduction reaction. *J. Mater. Chem. A* **2017**, *5*, 2073–2082. [[CrossRef](#)]
136. Li, O.L.; Chiba, S.; Wada, Y.; Lee, H.; Ishizaki, T. Selective nitrogen bonding states in nitrogen-doped carbon via a solution plasma process for advanced oxygen reduction reaction. *RSC Adv.* **2016**, *6*, 109354–109360. [[CrossRef](#)]
137. Panomsuwan, G.; Chiba, S.; Kaneko, Y.; Saito, N.; Ishizaki, T. In situ solution plasma synthesis of nitrogen-doped carbon nanoparticles as metal-free electrocatalysts for the oxygen reduction reaction. *J. Mater. Chem. A* **2014**, *2*, 18677–18686. [[CrossRef](#)]
138. Panomsuwan, G.; Saito, N.; Ishizaki, T. Electrocatalytic oxygen reduction on nitrogen-doped carbon nanoparticles derived from cyano-aromatic molecules via a solution plasma approach. *Carbon* **2016**, *98*, 411–420. [[CrossRef](#)]
139. Morishita, T.; Ueno, T.; Panomsuwan, G.; Hieda, J.; Yoshida, A.; Bratescu, M.A.; Saito, N. Fastest Formation Routes of Nanocarbons in Solution Plasma Processes. *Sci. Rep.* **2016**, *6*, 36880. [[CrossRef](#)]
140. Ishizaki, T.; Chiba, S.; Kaneko, Y.; Panomsuwan, G. Electrocatalytic activity for the oxygen reduction reaction of oxygen-containing nanocarbon synthesized by solution plasma. *J. Mater. Chem. A* **2014**, *2*, 10589–10598. [[CrossRef](#)]
141. Kondratowicz, I.; Nadolska, M.; Şahin, S.; Łapiński, M.; Przeźniak-Welenc, M.; Sawczak, M.; Yu, E.H.; Sadowski, W.; Żelechowska, K. Tailoring properties of reduced graphene oxide by oxygen plasma treatment. *Appl. Surf. Sci.* **2018**, *440*, 651–659. [[CrossRef](#)]
142. Wong, C.H.A.; Sofer, Z.; Klímová, K.; Pumera, M. Microwave Exfoliation of Graphite Oxides in H<sub>2</sub>S Plasma for the Synthesis of Sulfur-Doped Graphenes as Oxygen Reduction Catalysts. *ACS Appl. Mater. Interfaces* **2016**, *8*, 31849–31855. [[CrossRef](#)] [[PubMed](#)]
143. Tian, Y.; Wei, Z.; Wang, X.; Peng, S.; Zhang, X.; Liu, W.-m. Plasma-etched, S-doped graphene for effective hydrogen evolution reaction. *Int. J. Hydrogen Energy* **2017**, *42*, 4184–4192. [[CrossRef](#)]
144. Zhou, J.; Qi, F.; Chen, Y.; Wang, Z.; Zheng, B.; Wang, X. CVD-grown three-dimensional sulfur-doped graphene as a binder-free electrocatalytic electrode for highly effective and stable hydrogen evolution reaction. *J. Mater. Sci.* **2018**, *53*, 7767–7777. [[CrossRef](#)]
145. Panomsuwan, G.; Saito, N.; Ishizaki, T. Electrocatalytic oxygen reduction activity of boron-doped carbon nanoparticles synthesized via solution plasma process. *Electrochem. Commun.* **2015**, *59*, 81–85. [[CrossRef](#)]
146. Li, X.; Li, H.; Li, M.; Li, C.; Sun, D.; Lei, Y.; Yang, B. Preparation of a porous boron-doped diamond/Ta electrode for the electrocatalytic degradation of organic pollutants. *Carbon* **2018**, *129*, 543–551. [[CrossRef](#)]
147. Panomsuwan, G.; Saito, N.; Ishizaki, T. Simple one-step synthesis of fluorine-doped carbon nanoparticles as potential alternative metal-free electrocatalysts for oxygen reduction reaction. *J. Mater. Chem. A* **2015**, *3*, 9972–9981. [[CrossRef](#)]

148. Tian, Y.; Mei, R.; Xue, D.-Z.; Zhang, X.; Peng, W. Enhanced electrocatalytic hydrogen evolution in graphene via defect engineering and heteroatoms co-doping. *Electrochim. Acta* **2016**, *219*, 781–789. [[CrossRef](#)]
149. Lee, S.; Heo, Y.; Bratescu, M.A.; Ueno, T.; Saito, N. Solution plasma synthesis of a boron–carbon–nitrogen catalyst with a controllable bond structure. *Phys. Chem. Chem. Phys.* **2017**, *19*, 15264–15272. [[CrossRef](#)]



© 2019 by the authors. Licensee MDPI, Basel, Switzerland. This article is an open access article distributed under the terms and conditions of the Creative Commons Attribution (CC BY) license (<http://creativecommons.org/licenses/by/4.0/>).